NTNU
Norwegian University of
Science and Technology

In-plane Fracture Front Propagation in the Thin Plate Fiber Bundle Model

Jørgen Vågan

Master of Science in Physics and Mathematics
Submission date: June 2016
Supervisor: Alex Hansen, IFY

Norwegian University of Science and Technology
Department of Physics

To all my fellow students who have helped me through this course of study

Abstract

A new history independent thin plate Fiber Bundle Model is derived in order to model in-plane material fracture. The model provides an easy way of studying the not yet fully understood fracture processing zone.

Only considering relatively small system sizes, the model seems to be consistent with experimental observations, giving a large scale roughness exponent of

$$\zeta_{large} = 0.27 \pm 0.06.$$

No direct value was obtained for the small scale regime. However, its behavior and estimated fractal dimension is believed to be consistent with a small scale roughness exponent,

$$\zeta_{small} = 2/3,$$

described by gradient percolation.

The high velocity tail of the velocity distribution of the fracture front, seemed to be consistent with a power law with an exponent of

$$\eta_{sim} = -0.75 \pm 0.07.$$

This is, however, not consistent with the experimental value of $\eta_{exp} = -2.55 \pm 0.15$.

Sammendrag

En ny historieuavhangig fiberbundtmodell, modellert som en tynn plate, er kontruert for å beskrive sprekkvekst langs et plan. Modellen utgjør en enkel måte å studere sprekkprosess-sonen på, en region nær tuppen på en sprekk, som enda ikke er helt forstått.

For relativt småsystemer klarer modellen ågjennskape resultater som er konsistent med experimentelle observasjoner, og gir en ruhetseksponent på

$$\zeta_{large} = 0.27 \pm 0.06,$$

i storskalaregimet. Ingen spesifikk verdi ble oppnåd for ruhetseksponenten for småskalaregime, men resultatene tyder på å være konsistente med en ruhetseksponent på

$$\zeta_{small} = 2/3,$$

beskrevet av gradientperkulasjon.

De høye hastighetene i hastihetsfordelingen av sprekkveksten, virket til å være i sammsvar med en potenslov med en eksponent på

$$\eta_{sim} = -0.75 \pm 0.07.$$

Dette er desverre ikke konsitent med den experimentelle verdien $\eta_{exp} = -2.55 \pm 0.15$.

Preface

This thesis is written under the supervision of Professor Alex Hansen at the Department of Physics and is the last part of my Master's degree at the Norwegian University of Science and Technology. This Master's Thesis is a study of the in-plane roughness exponent for a thin plate Fiber Bundle Model and is equivalent to half an academic year, corresponding to 30 ECTS credits.

The study was conducted with no prior knowledge on the subject, made possible only through the help of dedicated and helpful colleges. For those who are not as lucky, this thesis tries to explain some of the concepts more thoroughly and contains a lot of illustrations. In addition, the introduction tries to dive, fairly quickly, into the world of fracture mechanichs and Fiber Bundle Models by starting from the big picture. This hopefully provides both the motivation and the context of the problem, which will be properly formulated at the end of the introduction.

Trondheim, June 17, 2016

Jørgen Vågan

Acknowledgement

First, I would like to thank Professor Alex Hansen for his supervision, advice and for providing such an interesting and fun project for my Master's Thesis. Secondly, I would like to thank the Department of Physics for providing me with additional computational resources, which were sorely needed due to the highly, computationally expensive problem faced using this model. I would also like to thank Knut Jørgen Måløy and Norsk Oljemuseum for allowing me to use their photos.

Personally, I would especially like to thank all the M.Sc. and Ph.D. students of my research group; Magnus Dahle, Håkon Nygård, Eivind Bering, Morten Vassvik and Jonas Kjellstadli, for all their help and consultation. Without your help, this thesis would not have been possible. You have helped make this project the most enjoyable thing I have ever done during my time here at NTNU. I would also like to thank Knut Magnus Kvamtrø, who in the earlier days dedicated much time helping me with the introductionairy programming courses, and gave the foundation for a numerical master's thesis; Jabir Ali Ouassou, for all the enthustiastic discussions, help and crazy stories; and Trygve Sørgård, for the good company and much required help during our year abroad.

Finally, I would also like to thank my girlfriend, Tiril, who have helped me alot through the writing process. Thank you for the support, patience and hours spent listening to all the fiber-bundle-model-rambling.

Acronyms and Abbreviations

LEFM	Linear Elastic Fracture Mechanics
NLEFM	Non-Linear Fracture Mechanics
EPFM	Elaso-Plastic Fracture Mechanics
MD	Molecular Dynamics
FBM(s)	Fiber Bundle Model(s)
SCFBM	Soft Clamp Fiber Bundle Model
ELS	Equal Load Sharing
LLS	Local Load Sharing
WTM	Waiting Time Matrix
RNG	Random Number Generator

Nomenclature

$p(t)$	Probability Density Function
$P(t)$	Cumulative Probability Density Function
N	Number of Fibers in Bundle
k	Number of Broken Fibers in Bundle
t_i	Threshold of Fiber i
κ	Elastic Spring Constant
F	Applied Force on Bundle
σ	Bundle Strain Divided by Initial Bumber of Fibers
σ_i	Local Strain on Fiber i
s_{ij}	Cluster Size (LLS)
p_{ij}	Perimeter Length (LLS)
N_x	Number of Fibers in the x-direction, i.e. the System Length
N_y	Number of Fibers in the y-direction, i.e. the System Width
λ	Mass Density of the Beams
B	Bending Rigidity of the Beams
a	Lattice Constant
z	Clamp Deformation
d_{ij}	Clamp Deformation at Fiber (i,j) in the 2D Bridge Model
g	Gravitational Acceleration
f	Force Density
f_{ij}^m	Force on Beam m from Beam-Coupling at the ij'th Node
f_{ij}	Third Power Coefficient of the y-directed Subsolutions
ζ_{ij}	Dimensionless Coupling Force between Beams
α	Dimensionless Gravity
α_L	Dimensionless Edge Load
β	Dimensionless Spring Constant

ζ	In-Plane Roughness Exponent
D_{if}	Fractal Dimension of the Intact Fracture Front
D_{bf}	Fractal Dimension of the Broken Fracture Front
n_{if}	Length of the Intact Front
n_{bf}	Length of the Broken Front
x_{if}	Position of the Intact Fracture Front
x_{bf}	Position of the Broken Fracture Front
$\tilde{x}_f$	Average Position of the Intact and Broken Fracture Front
x_f	Weighted Average Position of the Fracture Front
w_{if}	Width of the Intact Fracture Front
w_{bf}	Width of the Broken Fracture Front
$\tilde{w}_f$	Average Width of the Intact and Broken Fracture Front
w_f	Weighted Average Width of the Fracture Front
ρ	Scaling function (*Family-Vicsek scaling relation*)
b	Growth Exponent
Z	Dynamic Exponent
v_{ij}	Fracture Front Velocity at Position (i,j) (the ij'th Element of Spatiotemporal Velocity Map)
$\langle v \rangle$	Global Average Velocity $\left(\sum_{ij} v_{ij} p(v_{ij})\right)$
$V_{C,bf}$	Threshold Velocity Map of the Broken Fracture Front
η	Velocity Distribution Depinning Exponent

Table of Contents

List of Tables

List of Figures

Chapter 1

Introduction

Failure; an important topic in most technological branches of both engineering and science. Due to uncertainties, damaged or defective materials, or inadequacies in construction, failure is likely to occur. Given a building, an aircraft or a vessel, it would clearly be a disaster if it were to fall apart during use. For example on January 16, 1943, the tanker SS Schenectady nearly broke in half as cold weather embrittled the steel of the hull [1]. A more tragic example is the oil rig platform Alexander L. Kielland, shown in Figure 1.1. The platform capsized during a storm as a result of fatigue failure in its lower tubular bracing [2]. These examples demonstrate how

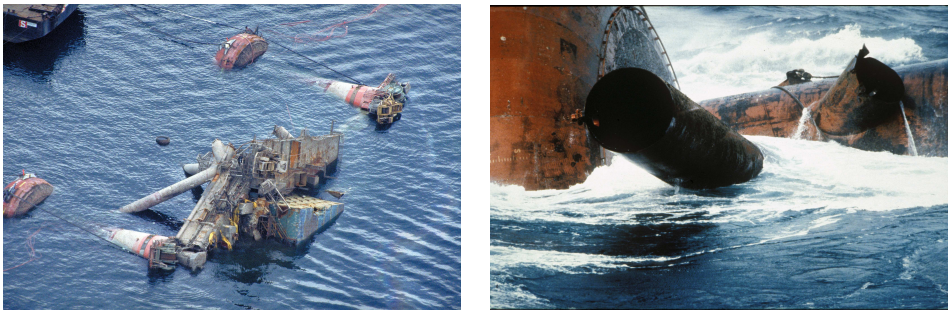

(a) **(b)**

Figure 1.1: On March 27, 1980, the platform Alexander L. Kielland, shown in **(a)**, capsized. **(b)** shows the fractured D6 bracing attached to the D leg, which broke off during the accident. The material, welding and expected endurance of the bracing was considered to be inadequate [2]. Foto: ConocoPhillips/Norsk Oljemuseum.

important it is to keep material fracture under control. However, preventing fracture is a technology of its own and in order to effectively design against it, one needs to understand the fundamental processes behind it. This is not an easy task, as material fracture is a complex process and there are several ways a material might break apart. For instance, all real fracture processes can be described by a mix of three ideal fracture modes, see Figure 1.2. In physics research, predominantly mode I is used, because, in contrast to

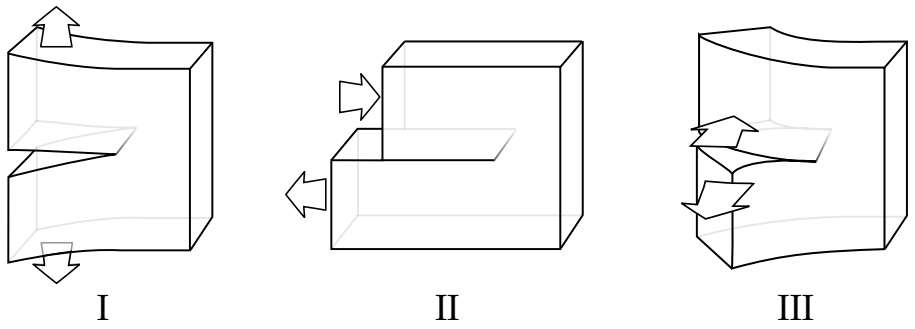

Figure 1.2: The three modes of fracture: mode I, opening or tension; mode II, sliding or in-plane shear; and mode III, tearing or out-of-plane shear. The figure is adapted from [3].

mode II and III, it does not wear down the fracture surface, which serves as a footprint of the fracture process.

The fractured surface left behind can also vary in complexity, depending on the geometry of the physical system. This is illustrated in Figure 1.3. Here, the tip, or front, of the crack is shown as a point moving in the plane, a curve moving in the plane, or a curve moving through space. The fractured surface left behind after the propagating front, is extremely rough and irregular. In 1984, its complexity was described by Mandelbrot as being *fractal*, as its morphology seemed similar on many length scales [4]. However, the fracturing front itself was not directly studied until 1997, when Schmittbuhl and Måløy [5] managed to constrain the crack growth to a weak plane consistent with the two-dimensional geometry given in Figure 1.3. This was obtained by annealing together two Plexiglas plates with rough surfaces, obtained through sandblasting. The sandblasting also made the otherwise transparent surface of the Plexiglas plates opaque, and created a visual dis-

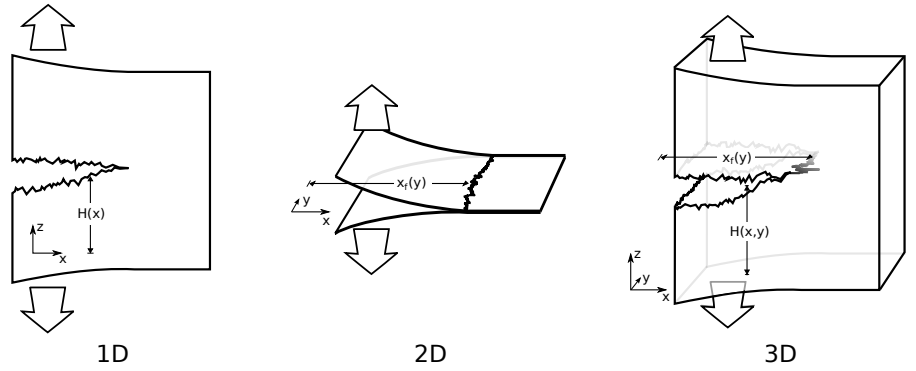

Figure 1.3: The fracture geometry of a mode I fracturing process in one-, two- and three dimensions. $H(x)$ describes the fracture surface left behind and $x_f(x)$ describes how far the fracture front has propagated into the system. The figure is adapted from [3].

tinction between the intact transparent annealed surface and the fractured surface. This together with the transparency of the Plexiglas plates, allowed for the first direct observation of the fracture front, the border between contact and non-contact region [5]. A sketch of the experimental setup is given in Figure 1.4. After this, further research on in-plane fracture have been conducted using the same experimental setup. For instance, a dynamical survey has been conducted by Tallakstad et al. [6]. More interestingly, by using a larger experimental setup that earlier, Santucci et al. [7] managed to show that there could be two different fracturing processes at work, based on the morphology of the front, one dominating on small length scales, and one dominating on large scales.

There exists numerous ways to describe the fracture of materials theoretically. Examples of this are linear elastic fracture mechanics (LEFM), non-linear elastic fracture mechanics (NLEFM) and elasto-plastic fracture mechanics (EPFM). LEFM treats the material as a continuous medium with linear elastic properties [8, p.5]. The accuracy of the description can be increased by introducing non-linear or plastic, irreversible deformation using NLEFM or EPFM, respectively. LEFM, NLEFM and EPFM are all macroscopic theories. When they are used to study the crack front of a fracturing process, it is referred to as a top-down approach [8, p.5]. These theories

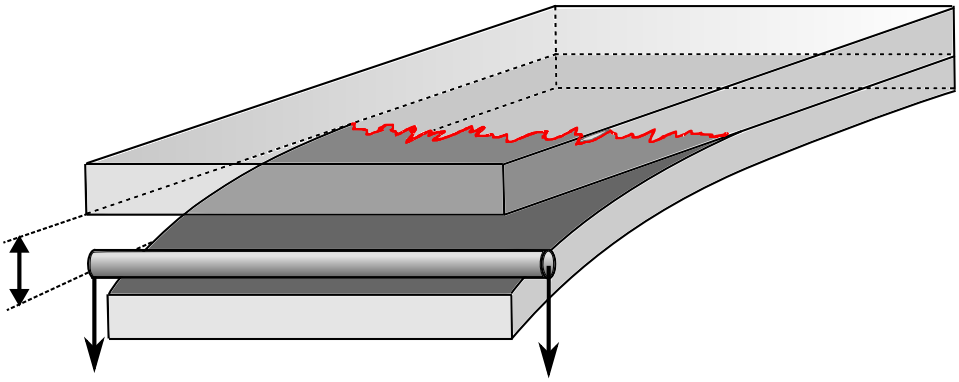

(a)

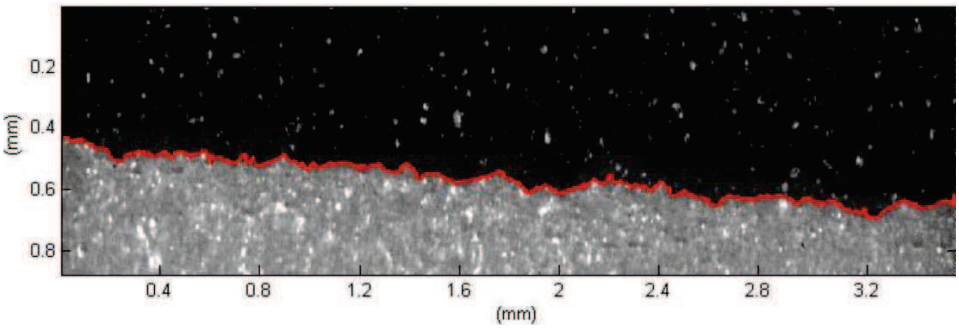

(b)

Figure 1.4: **(a)** A sketch of the experimental setup of Schmittbuhl and Måløy together with **(b)** a image of the fracture front from the experiments. Photo: K.J. Måløy.

are so far not able to sufficiently describe the high stress region close to the fracture tip, giving the fracture front [3]. However, with the dramatic rise of computational processing power, materials can now be modelled as ensembles of interacting atoms and molecules, and is called Molecular Dynamics (MD) [8, p.5]. Although MD is computationally expensive, it provides an alternative method of studying the fracturing front.

There is also a third option, which, compared to MD, provides a much faster and easier way to study the fracture front. This approach treats the material as a set of irreversibly breakable fibers, called a Fiber Bundle Model (FBM). Regardless of their simplicity, FBMs show an extraordinary rich-

ness in behaviors [8, p.8] and can be defined with varying complexity [9]. A few years ago, Gjerden did a numerical analysis using a FBM treating the material response to that of an elastic thick plate. This model is referred to as the Soft Clamp Fiber Bundle Model (SCFBM) [10, 11], and managed to recreate the behavior seen experimentally on both scales [3].

Problem Formulation

Encouraged by this result, this Thesis sets to out to derive a thin plate FBM, consistent with the experimental setup of Schmittbuhl and Måløy. In addition, it should be investigated whether or not the thickness makes a difference, by comparing it to the results obtained from the thick plate SCFBM used by Gjerden. The thin plate FBM is to be based on the one-dimensional Bridge FBM developed last year by Nygård [12]. Practically, this means to find a way to extend the Bridge FBM to two dimensions and find the appropriate boundary conditions to obtain a mode I, in-plane fracture propagation. A sketch of the final model to be derived is given in Figure 1.5. Because the model considered in this Thesis is a FBM, a more theoretical

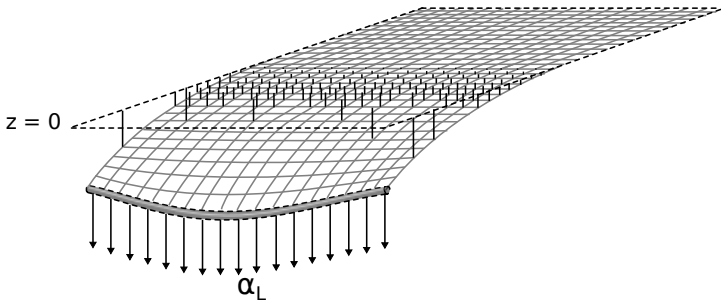

Figure 1.5: A stiff plate is constructed from a 2D grid of Eurler-Bernoulli beams and is loaded vertically from one end. The vertical lines represent the extended fibers of the bundle.

introduction to FBMs will be given in 2.1. The complete derivation of the thin plate Bridge FBM will be given in 2.2. Before any comparison can be made, the required terminology and quantitative experimental results must be presented. This will be done in Section 2.4 and marks the end of the chapter. After this, Chapter 3 will present the methods and algorithms used to solve the problem. Finally, Chapter 4, 5 and 6 provides the results, discussion and conclusion, respectively.

Chapter 2

Theoretical Description

This chapter will begin by giving a proper introduction to FBMs and the fundamental but simple models named the Equal Load Sharing and Local Load Sharing FBM. After this, Section 2.2 will provide the theoretical derivation of the thin plate FBM to be investigated and compared with the experimental results.

2.1 Introduction to fiber bundle models

The modern history of FBMs began in 1926 when Fredrick Thomas Peirce tried to model the strength of cotton yarns [13] and in 1945, Daniels took the fiber bundle model and treated it as a problem of statistics rather than material science [14]. In his paper, the bundle is treated as a set of linearly elastic fibers that are laid out in parallel and connects two clamps, see Figure 2.1. The clamps are pulled apart from each other and give rise to stresses on each individual fiber. Each fiber is assigned an individual threshold value t_i, chosen from some probability density $p(t)$. When the fiber is elongated beyond this threshold value, the fiber fails and can no longer carry any force. When a fiber breaks, its load is redistributed to some subset of the remaining fibers, usually in a way that can be physically interpreted as deformations in the clamps due to the absence of the failed fiber [8]. Figure 2.2 illustrates some physical interpretations of the equal load sharing, local load sharing and the Bridge model. This will be explained in more detail in Section 2.1.3.

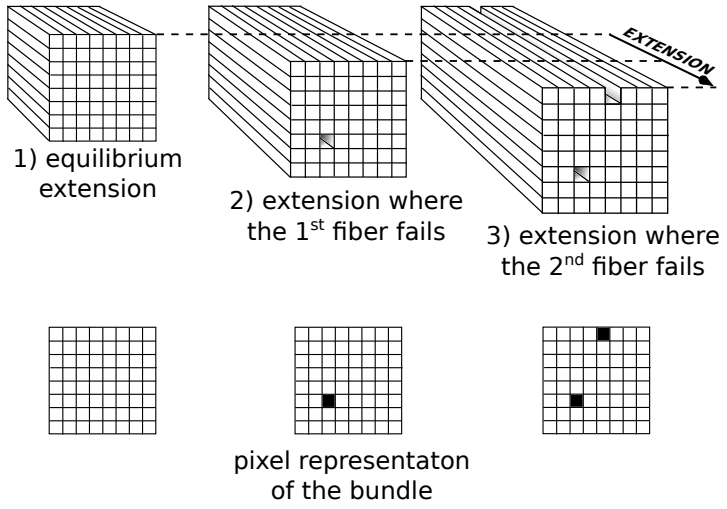

Figure 2.1: A simple example of a classical fiber bundle model of fibers assembled in a square lattice parallel to one another. The fiber bundle is stretched until the fibers break one by one. The failed fibers are effectively removed from the bundle. The figure was inspired by [9].

The models presented in this thesis are all simple, history independent and

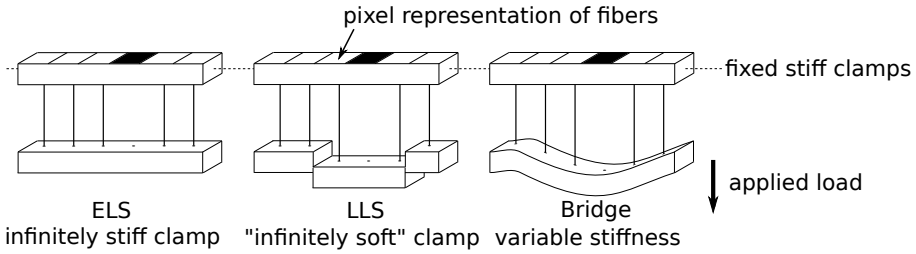

Figure 2.2: Physical interpretation of the equal load sharing, local load sharing and bridge FBM. When looking at two equally soft clamps, one can for symmetry reasons replace one of them with an infinitely stiff clamp without changing the result of the system [8, p.113].

only assume simple fibers following Hookean elasticity up to the breaking point. When the fibers break, they break irreversibly and are effectively

removed from the bundle, see Figure 2.1. Mathematically speaking, this is equivalent to describing fiber i by a spring constant

$$\kappa_i = \begin{cases} \kappa & \text{for intact fiber} \\ 0 & \text{for broken fiber} \end{cases} \tag{2.1}$$

Notice that all intact fibers of the model are given the same spring constant κ. This is done for all the FBM presented in this thesis.

2.1.1 The threshold distribution

The probability density $p(t)$, from which the thresholds are drawn, is usually denoted by its cumulative distribution function $P(t)$ and is known as the *threshold distribution* [15, p.27]

$$\text{Prob}(t_i < t) = P(t) = \int_0^t p(u)du, \tag{2.2}$$

The threshold distribution provides a random element in the system. This randomness makes every instance of the fracturing process different. Through statistical evaluation of ensembles of such systems, one can draw conclusions on the common behavior emerging from sample fluctuations and averages. Examples of typical threshold distributions are the uniform threshold distribution [15, p.28]

$$P(t) = \begin{cases} t/t_r & \text{for} \quad 0 \leq t \leq t_r \\ 1 & \text{for} \quad t > t_r \end{cases} \tag{2.3}$$

and exponential distribution

$$P(t) = \int_{t_0}^t e^{t_0 - t'} dt' = 1 - e^{t_0 - t}, \qquad t_0 \leq t < \infty, \tag{2.4}$$

where t_r is a constant giving the maximal theshold value and t_0 is the so-called cut-off parameter.

2.1.2 Strain curves

If the bundle consists of N fibers and is affected by an externally applied force F, the stress is usually denoted by the applied force scaled by the

initial number of fibers $\sigma = F/N$. There are two different approaches to control the fracturing process of the bundle. One way is to increase the force in steps until all the fibers in the bundle have failed. This is known as *force controlled loading*, as the external force is the control parameter. The drawback of this method is that the number of fibers that breaks, if any, depends on the size of the force step used. Using large steps gives loss of information of the fracturing process, while small steps could introduce unnecessary iterations where nothing happens. The latter would pose a huge problem for the model presented in this thesis due to the large computational time of every iteration. This is avoided when using *strain controlled loading* due to the linear relationship between the stress and strain of the bundle. Here, the extension of the bundle, or strain, is the controlling parameter. The strain is increased until a single fiber breaks, and before another fiber manages to break, the extension is set to zero. This is called *quasistatic loading* [8, p.72] and is repeated until all the fibers of the system have failed. The force felt by the failing fibers at the threshold extension gives the *strain-curve*, showing the strain σ as a function of the number of failed fibers k.

2.1.3 Force distribution, ELS and LLS

The load redistribution of a failing fiber to the remaining fibers can be modelled in different ways. Two key models in this field, named after how they redistribute the forces, are called the equal load sharing (ELS) model and the local load sharing (LLS) model. If k of the N initial fibers have failed, then ELS gives a loading of

$$\sigma = \frac{1}{N}(N-k)\kappa z \tag{2.5}$$

for the extension z which is divided equally among all the $N-k$ surviving fibers. The equal load sharing quality neglects any bias for some fibers to break over others, and leave the the system independent of both system size and dimensionality. This means that given the thresholds of the fibers, the strain-curve

$$\sigma = \left(1 - \frac{k}{N}\right)\kappa \cdot \min_{i\in\Omega}\{t_i\} \tag{2.6}$$

would be the same in one dimension as if the fibers were laid out in two dimensions. Here Ω denotes the set of thresholds of the remaining fibers.

The physical interpretation of this, at least in one- and two dimensions, is that the clamps at each end are infinitely stiff. This is illustrated in Figure 2.3.

In LLS on the other hand, the load of nearest-neighbor connected bro-

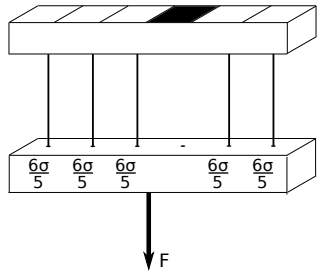

Figure 2.3: ELS force distribution of the applied strain σ; all surviving fibers share the bundle strain equally.

ken fibers, called clusters or holes, is redistributed only to the intact nearest neighbors forming the perimeter of the cluster. This is illustrated in Figure 2.4 for one dimension, where the perimeter of a hole is maximally of size 2. The force σ_j on a fiber j in the perimeter of a hole thus becomes [16, 17]

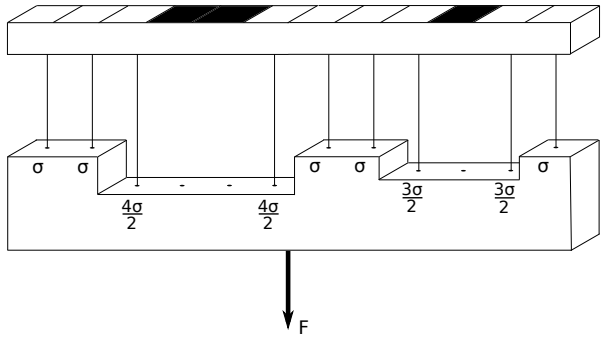

Figure 2.4: LLS force distribution of the applied force σ. The deformation due to a hole can be illustrated as a discrete drop given by the number of broken fibers of the hole.

$$\sigma_j = \left(1 + \sum_m \frac{s_{jm}}{p_{jm}}\right)\sigma, \tag{2.7}$$

where m denotes all neighboring holes of the fiber, s_{jm} the number of broken fibers in the m'th hole, and p_{jm} the size of its perimeter, which fiber j is a part of. All fibers not being part of any perimeter of a hole remains unaffected of the failing fibers, and just feel the scaled applied force σ. One may verify that the sum over all fibers gives $\sum_j \sigma_j = N\sigma = F$. Due to how the LLS model distributes forces, there is a bias for breaking fibers in the vicinity of holes and the strain curve is obtained using the *breaking criterion* [8, p.72]

$$\max_j \left(\frac{\sigma_j}{t_j}\right), \tag{2.8}$$

which will also be important for how the fibers are broken in the following model. A more thorough explanation of Eq. (2.8) is given in the Appendix, A. Continuing, Eq. (2.7) can be rewritten in terms of the applied force, giving the LLS strain curve

$$\sigma = \kappa t_j \left(1 + \sum_m \frac{s_{jm}}{p_{jm}}\right)^{-1}, \tag{2.9}$$

where t_j is the threshold satisfying the breaking criterion given in Eq. (2.8). LLS can to some degree be physically interpreted as the clamps being infinitely soft, at least in one dimension. In this way, ELS and LLS mark the two extremes: One representing an infinitely stiff clamp and distributes forces globally, while the other is extremely soft and only distributes the forces locally.

In certain regions of the fracturing process, LLS still tend to behave similar to ELS. If one considers the beginning of a rupturing process, the fibers tend to break because they are weak, and not because they are part of the perimeter of a hole. Choosing the exponential threshold distribution, Eq. (2.4), and varying the cut-off parameter t_0, one can control the relative strength of the fibers, and force the fracturing process to either be unlocalized like in ELS, or localized, which means that only fibers part of a perimeter break [16]. Sinha, Kjellstadli and Hansen [18] also showed that the behavior of LLS

approaches ELS as the dimension of the problem approaches infinity.
To recap, this section has covered two models representing either infinite or only local interaction bewteen the fibers of the bundle. However, the model introduced in the following chapter represents a clamp of variable stiffness and a finite, tunable range of interaction.

2.2 The Bridge fiber bundle model

In 2015, Nygård introduced a new, one-dimensional FBM named the Bridge Fiber Bundle Model [12], bearing the resemblance of a hanging bridge, illustrated in Figure 2.5. The model distributes forces through a deforming clamp modelled by a one-dimensional beam with bending rigidity B. The thin plate model derived in this section will be an extension of the Bridge Model from one to two dimensions. For this reason, it is only natural to start by introducing the one-dimensional Bridge Model first and then generalize it to two dimensions, as many of the relations are the identical and can be reapplied.

2.2.1 Introduction: the One-dimensional Bridge Model with Periodic Boundary Conditions

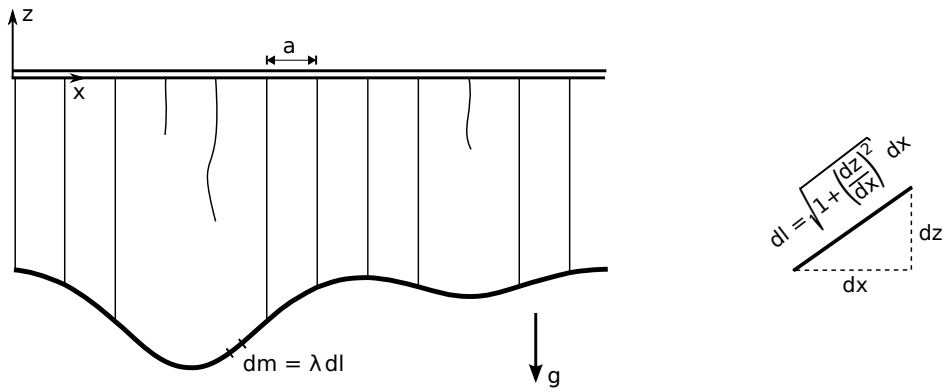

Figure 2.5: The one-dimensional Bridge Model with periodic boundary conditions.

The system consists of N fibers located at $x_i = ia$ for $i \in [0, N-1]$, with lattice spacing a. The fibers are supporting a beam with uniform mass density λ. The boundaries are chosen to be periodic, such that $x_0 = x_N$. Given a force density $f(x)$, the beam will deform with deflection $z(x)$ according to

$$B\frac{d^4z}{dx^4} = f(x). \tag{2.10}$$

The two contributions to the force density are the gravitational force density,

$$f_g(x) = -g\lambda\sqrt{1 + \left(\frac{dz}{dx}\right)^2}, \tag{2.11}$$

and the forces from the elastic fibers

$$f_\kappa(x) = \sum_{i=0}^{N-1} \kappa_i \big[z_0 - z(x_i)\big]. \tag{2.12}$$

In the above equations, g is the gravitational acceleration, z_0 is the unloaded length of the fibers, and, like in ELS and LLS, κ_i is the Hookean spring constant of fiber i such that

$$\kappa_i = \begin{cases} \kappa, & \text{for intact fibers;} \\ 0, & \text{for broken fibers.} \end{cases}$$

For simplicity, the threshold values of the fibers are picked out of a uniform threshold distribution, Eq. (2.3), with $t_r = 1$.

Inserting $f(x) = f_\kappa(x) + f_g(x)$ in Eq. (2.10), the gravitational term Eq. (2.11) poses the problem of making the equation non-linear. However, for a very stiff system it can be assumed that the beam does not bend that easily, and the slope of the beam can be assumed to be so small that the term can be Taylor expanded to first order, such that

$$f_g = \lambda g. \tag{2.13}$$

Now, by introducing the dimensionless constants

$$\alpha = \frac{g\lambda a^3}{B} \qquad\qquad \beta_i = \frac{\kappa_i a^3}{B}$$

Eq. (2.10) can be rewritten on a dimensionless form

$$\frac{d^4 z}{dx^4} = -\alpha + \sum_{i=0}^{N-1} \beta_i \big[z_0 - z(x)\big]\delta(x - i). \tag{2.14}$$

Keep in mind that the spatial variables x and z in the above equation are rescaled with the lattice spacing a. Because our system is subject to a piecewise continuous load, the solution to Eq. (2.14) may be written on the form [19]

$$z(x) = z_0(x) + \sum_{i=0}^{N-1} \theta(x - x_i)\big[z_{i+1}(x) - z_i(x)\big], \tag{2.15}$$

where θ is the Heaviside function. Do not confuse $z_0(x)$ above with the unloaded length z_0 of the fibers given in Eq. (2.14). From now on z_0 is set to zero for simplicity. To further simplify calculations, the domain of the sub solutions $z_i(x)$ in Eq. (2.15) is shifted from $[i, i+1]$ to $[0, 1]$, by mapping x to $x - i$. In this way, all the solutions $z_i(x)$ are given by $x \in [0, 1]$ with $x = 0$ denoting the left boundary of the solutions, while $x = 1$ denotes the right boundary.
Now, between fiber i and $(i + 1)$, the system is only affected by gravity

$$\frac{d^4 z_i}{dx^4} = -\alpha,$$

and the solution between fibers can be solved through integration, giving

$$z_i(x) = -\frac{\alpha}{24}x^4 + a_i x^3 + b_i x^2 + c_i x + d_i, \tag{2.16}$$

where a_i, b_i, c_i and d_i are constants of integration. In order to decide the integration constants, the boundaries need to be taken into account. The i'th fiber is located at the i'th solution's left boundary. With $z_0 = 0$ the deflection at the i'th fiber is governed by

$$\frac{d^4 z_i}{dx^4} = -\alpha - \beta_i z(x)\delta(x - i). \tag{2.17}$$

Integrating Eq. (2.17) over the interval $[i-\epsilon, i+\epsilon]$, one, two, three and four times and taking the limit $\epsilon \to 0$ for each of them, results in the following four equations

$$\left.\frac{d^3 z_i}{dx^3}\right|_{x=0} - \left.\frac{d^3 z_{i-1}}{dx^3}\right|_{x=1} = \beta_i z_i \tag{2.18a}$$

$$\left.\frac{d^2 z_i}{dx^2}\right|_{x=0} - \left.\frac{d^2 z_{i-1}}{dx^2}\right|_{x=1} = 0 \tag{2.18b}$$

$$\left.\frac{dz_i}{dx}\right|_{x=0} - \left.\frac{dz_{i-1}}{dx}\right|_{x=1} = 0 \tag{2.18c}$$

$$\left.z_i\right|_{x=0} - \left.z_{i-1}\right|_{x=1} = 0, \tag{2.18d}$$

which gives a set of boundary conditions connecting $z_i(0)$ to $z_{i-1}(1)$. Now, plugging Eq. (2.16) into Eqs. (2.18) results in four equations

$$6a_{i-1} - 6a_i - \beta_i d_i = \alpha \tag{2.19a}$$

$$6a_{i-1} + 2b_{i-1} - 2b_i = \frac{\alpha}{2} \tag{2.19b}$$

$$3a_{i-1} + 2b_{i-1} + c_{i-1} - c_i = \frac{\alpha}{6} \tag{2.19c}$$

$$a_{i-1} + b_{i-1} + c_{i-1} + d_{i-1} - d_i = \frac{\alpha}{24} \tag{2.19d}$$

connecting the coefficients a_i, b_i, c_i and d_i of Eq. (2.16) to the coefficients , a_{i-1}, b_{i-1}, c_{i-1} and d_{i-1}, of the previous solution. With periodic boundaries, there is N connection points at each fiber resulting in an equation system of $4N$ equations and $4N$ unknown coefficients. The system of equations, Eqs. (2.19), can equivalently be expressed in terms of a $4N \times 4N$ matrix

$$\begin{bmatrix}
-6 & & & -\beta_i & & & & & & & & & \cdots & 6 & & & \\
 & -2 & & & & & & & & & & & \cdots & 6 & 2 & & \\
 & & -1 & & & & & & & & & & \cdots & 3 & 2 & 1 & \\
 & & & -1 & & & & & & & & & \cdots & 1 & 1 & 1 & 1 \\
6 & & & & -6 & & & -\beta_i & & & & & \cdots & & & & \\
6 & 2 & & & & -2 & & & & & & & \cdots & & & & \\
3 & 2 & 1 & & & & -1 & & & & & & \cdots & & & & \\
1 & 1 & 1 & 1 & & & & -1 & & & & & \cdots & & & & \\
 & & & & 6 & & & & -6 & & & -\beta_i & \cdots & & & & \\
 & & & & 6 & 2 & & & & -2 & & & \cdots & & & & \\
 & & & & 3 & 2 & 1 & & & & -1 & & \cdots & & & & \\
 & & & & 1 & 1 & 1 & 1 & & & & -1 & \cdots & & & & \\
\vdots & \vdots & \vdots & \vdots & \vdots & \vdots & \vdots & \vdots & \vdots & \vdots & \vdots & \vdots & \ddots & & & & \\
 & & & & & & & & & 6 & & & & -6 & & & -\beta_i \\
 & & & & & & & & & 6 & 2 & & & & -2 & & \\
 & & & & & & & & & 3 & 2 & 1 & & & & -1 & \\
 & & & & & & & & & 1 & 1 & 1 & 1 & & & & -1
\end{bmatrix}
\begin{bmatrix} a_0 \\ b_0 \\ c_0 \\ d_0 \\ a_1 \\ b_1 \\ c_1 \\ d_1 \\ a_2 \\ b_2 \\ c_2 \\ d_2 \\ \vdots \\ a_{N-1} \\ b_{N-1} \\ c_{N-1} \\ d_{N-1} \end{bmatrix}
=
\begin{bmatrix} \alpha \\ \alpha/2 \\ \alpha/6 \\ \alpha/24 \\ \alpha \\ \alpha/2 \\ \alpha/6 \\ \alpha/24 \\ \alpha \\ \alpha/2 \\ \alpha/6 \\ \alpha/24 \\ \vdots \\ \alpha \\ \alpha/2 \\ \alpha/6 \\ \alpha/24 \end{bmatrix}.$$

which can be solved numerically. Two solutions for a $N = 5$ system is shown in Figure 2.6 This is in essence the 1D bridge model. Nygård [12] showed that when the system is fractured using α as the load parameter, β decides the stiffness of the system. In addition, he showed that the model approached ELS for $\beta \to 0$ and actet qualitatively like LLS for $\beta \approx 1$.

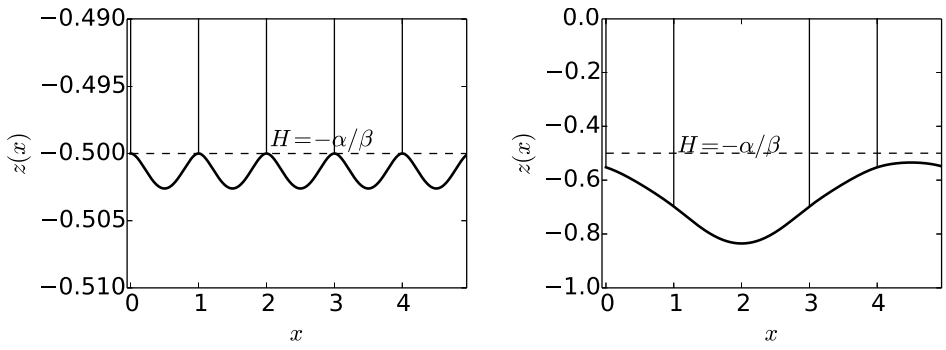

Figure 2.6: The shape of a $N = 5$ bridge model with periodic boundaries. The displacement of the bundle when all fibers are intact, shown in **(a)**, is given by the height $H = -\alpha/\beta$. **(b)** shows the same system but with the central fiber at $i = 2$ broken. The two closest fibers are more loaded than the two further away. The average height of all fibers is now given by $-5\alpha/4\beta$.

2.2.2 The Two-dimensional Thin Plate Bridge Model

The two-dimensonal Bridge Model derived in this section will consist of N_y x-directed beams layed out along the y-direction, and N_x y-directed beams layed out along the x-direction, creating a square grid of beams with lattice constant a, see Figure 2.7. A total of $N = N_x N_y$ fibers are connected to the system at each node. The intact fibers are considered to be elastic, with spring constant $\kappa_{ij} = \kappa$. At the ij'th node, beam i is connected to beam j, see Figure 2.8. The force on beam i, oriented in the x-direction, from beam i, is denoted f^x_{ij}. Likewise, because beam i is oriented in the y-direction, we set f^y_{ij} to denote the force on beam i from j. From Newton's third law, the forces should be equal in magnitude and oppositely directed

$$f^x_{ij} = -f^y_{ij} \tag{2.20}$$

The shape of the beams, z, is given by Eq. (2.10). The only difference compared to the one-dimensional case is the additional forces given in Eq. (2.20). The shapes of the x-directed beams are therefore

$$\frac{d^4 z^x_j}{dx^4}(x) = -\frac{g\lambda}{B} + \sum_{i=0}^{N_x-1} \left[\frac{\kappa_{ij}}{B} \left[z_0 - z^x_j(x) \right] + \frac{f^x_{ij}}{B} \right] \delta(x - ia), \tag{2.21}$$

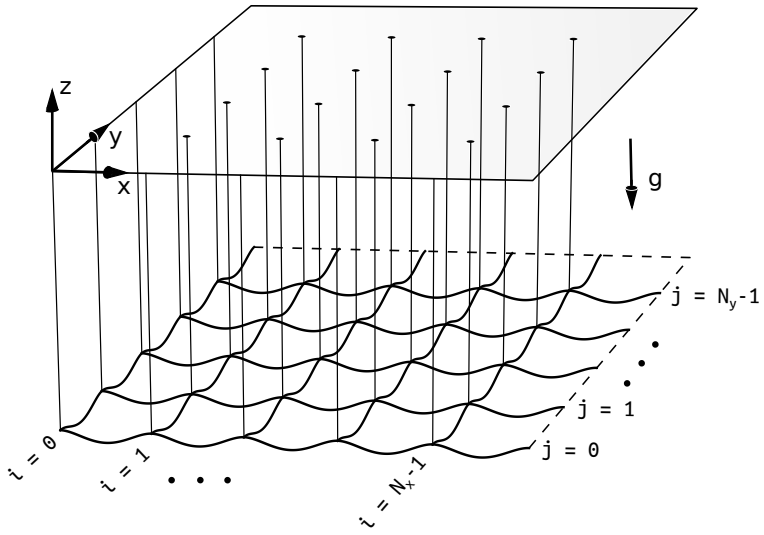

Figure 2.7: The 2D Bridge model consists of several Euler-Bernoulli beams layed out in a grid with fibers connected at each node. For this particular case it is shown fully intact with periodic boundary conditions.

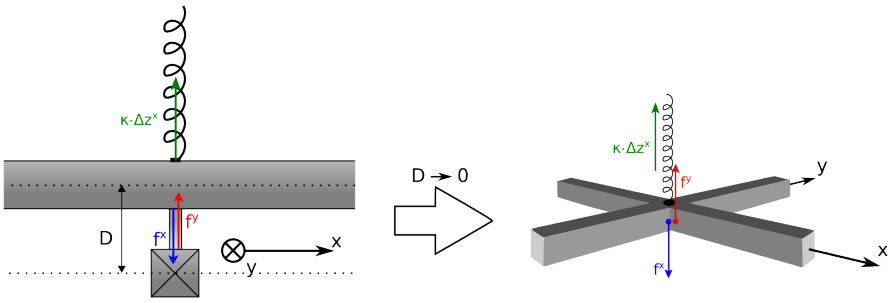

Figure 2.8: Beam j oriented along the x-direction is connected to fiber ij. Beam i, is connected to beam j. For intuition, picture a rigid rod of distance D such that $z_{ij}^x(0) - z_{ij}^x(0) = D$. Through the rod, the beams are acting with forces on each other in order to keep their separation D fixed. Allowing the rod, or more precisely the center to center length D between the beams, to go to zero the beams are essentially welded together, but the forces are assumed to be the same as with the case of the rod.

while the y-directed beams which are hanging from the x-directed beams follow

$$\frac{d^4 z_i^y}{dy^4}(y) = -\frac{g\lambda}{B} + \sum_{j=0}^{N_y-1} \frac{f_{ij}^y}{B}\delta(y - ja). \tag{2.22}$$

The forces in Eq. (2.21) and Eq. (2.22) is illustrated in Figure 2.8, respectively on the upper and lower beam. By introducing the dimensionless variables

$$\alpha = \frac{g\lambda a^3}{B} \qquad \beta_{ij} = \frac{\kappa_{ij} a^3}{B} \qquad \zeta_{ij} = \frac{f_{ij}^y a^2}{B} = -\frac{f_{ij}^x a^2}{B}, \tag{2.23}$$

Eq. (2.21) and Eq. (2.22) can be written on the dimensionless form

$$d_x^4 z_j^x(x) = -\alpha + \sum_{i=0}^{N-1} \big[-\beta_{ij} z_j^x(x) - \zeta_{ij} \big] \delta(x - i), \tag{2.24a}$$

$$d_y^4 z_i^y(y) = -\alpha + \sum_{j=0}^{N-1} \zeta_{ij}\delta(y - j). \tag{2.24b}$$

Here $d_x \equiv d/dx$, $d_y \equiv d/dy$ and the unloaded spring distance has been set to $z_0 = 0$ for simplicity.

Internal system

Treating Eq. (2.21) and Eq. (2.22) with exactly the same approach as in 1D, one obtains $2N$ subsolutions on the form

$$z_{ij}^x(x) = -\frac{\alpha}{24}x^4 + a_{ij}x^3 + b_{ij}x^2 + c_{ij}x + d_{ij}, \tag{2.25a}$$

$$z_{ij}^y(y) = -\frac{\alpha}{24}y^4 + e_{ij}y^3 + f_{ij}y^2 + g_{ij}y + h_{ij}, \tag{2.25b}$$

where Eq. (2.25a) gives the solution between fibers (i, j) and $(i+1, j)$, and Eq. (2.25b) is the solution between fibers (i, j) and $(i, j+1)$, see Figure 2.9.

By integration one finds 8 boundary conditions

$$d_x^3 z_{ij}^x(0) - d_x^3 z_{i-1,j}^x(1) = -\beta_{ij} z_j^x(0) - \zeta_{ij} \tag{2.26a}$$

$$d_x^2 z_{ij}^x(0) - d_x^2 z_{i-1,j}^x(1) = 0 \tag{2.26b}$$

$$d_x z_{ij}^x(0) - d_x z_{i-1,j}^x(1) = 0 \tag{2.26c}$$

$$z_{ij}^x(0) - z_{i-1,j}^x(1) = 0 \tag{2.26d}$$

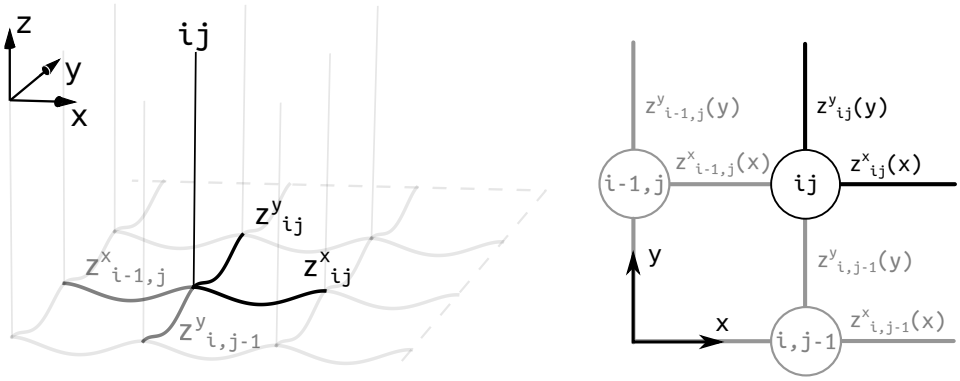

Figure 2.9: The layout of the subsolutions, $z^x_{ij}(x)$, $z^y_{ij}(y)$, $z^x_{i-1,j}(x)$ and $z^y_{i,j-1}(y)$, surrounding the ij'th fiber. Each fiber has two associated functions denoted by the same index: one function in the x-direction and one along the y-direction. Here the fibers are shown as vertical lines (left) or circular nodes (right).

$$d_y^3 z^y_{ij}(0) - d_y^3 z^y_{i,j-1}(1) = \zeta_{ij} \tag{2.26e}$$
$$d_y^2 z^y_{ij}(0) - d_y^2 z^y_{i,j-1}(1) = 0 \tag{2.26f}$$
$$d_y z^y_{ij}(0) - d_y z^y_{i,j-1}(1) = 0 \tag{2.26g}$$
$$z^y_{ij}(0) - z^y_{i,j-1}(1) = 0 \tag{2.26h}$$

4 for each direction, ensuring the discontinuities in the third derivative due to the point forces and continuity for the lower derivatives. Combining Eqs. (2.25) with Eqs. (2.26) and rearranging the terms, one ends up with

$$6a_{i-1,j} - 6a_{ij} - \beta_{ij} d_{ij} - \zeta_{ij} = \alpha \tag{2.27a}$$
$$6a_{i-1,j} + 2b_{i-1,j} - 2b_{ij} = \frac{\alpha}{2} \tag{2.27b}$$
$$3a_{i-1,j} + 2b_{i-1,j} + c_{i-1,j} - c_{ij} = \frac{\alpha}{6} \tag{2.27c}$$
$$a_{i-1,j} + b_{i-1,j} + c_{i-1,j} + d_{i-1,j} - d_{ij} = \frac{\alpha}{24} \tag{2.27d}$$

$$6e_{i,j-1} - 6e_{ij} + \zeta_{ij} = \alpha \tag{2.27e}$$

$$6e_{i,j-1} + 2f_{i,j-1} - 2f_{ij} = \frac{\alpha}{2} \tag{2.27f}$$

$$3e_{i,j-1} + 2f_{i,j-1} + g_{i,j-1} - g_{ij} = \frac{\alpha}{6} \tag{2.27g}$$

$$e_{i,j-1} + f_{i,j-1} + g_{i,j-1} + h_{i,j-1} - h_{ij} = \frac{\alpha}{24} \tag{2.27h}$$

The system of equations, Eqs. (2.27), contain 9 unknowns, but only 8 equations and is undetermined. However, all this set of equations does is to ensure continuity over fiber (i, j) in the x- and y-direction, respectively, like in the 1D model. What is missing is a constraint connecting the cables together into a coupled grid of beams, which is why the additional force variable ζ_{ij} is introduced. So far, there has only been established that there is a force present between the beams at each position (i, j) and that these two forces should be equal in magnitude and oppositely directed. Now, since continuity of the beams themselves is established through Eqs. (2.27), the beams in the x-direction can be coupled with the beams in the y-direction by demanding that

$$z_{ij}^{x}(0) = z_{ij}^{y}(0), \tag{2.28}$$

giving $d_{ij} = h_{ij}$. Inserting this into Eq. (2.25b), the resulting system of equations connecting the solutions around the internal fiber ij is therefore given as

$$6a_{i-1,j} - 6a_{ij} - \beta_{ij}d_{ij} - \zeta_{ij} = \alpha \tag{2.29a}$$

$$6a_{i-1,j} + 2b_{i-1,j} - 2b_{ij} = \frac{\alpha}{2} \tag{2.29b}$$

$$3a_{i-1,j} + 2b_{i-1,j} + c_{i-1,j} - c_{ij} = \frac{\alpha}{6} \tag{2.29c}$$

$$a_{i-1,j} + b_{i-1,j} + c_{i-1,j} + d_{i-1,j} - d_{ij} = \frac{\alpha}{24} \tag{2.29d}$$

$$6e_{i,j-1} - 6e_{ij} + \zeta_{ij} = \alpha \tag{2.29e}$$

$$6e_{i,j-1} + 2f_{i,j-1} - 2f_{ij} = \frac{\alpha}{2} \tag{2.29f}$$

$$3e_{i,j-1} + 2f_{i,j-1} + g_{i,j-1} - g_{ij} = \frac{\alpha}{6} \tag{2.29g}$$

$$d_{i,j-1} + e_{i,j-1} + f_{i,j-1} + g_{i,j-1} - d_{ij} = \frac{\alpha}{24}. \tag{2.29h}$$

This system now consists of 8 unknowns and 8 equations and is solvable. The solution in Figure 2.7 was found by solving an intact system with periodic boundaries. Like in the 1D case, the system of equations can be rewritten into a matrix. The number of $8N$ unknowns result in a $8N \times 8N$ sparse matrix. Each internal fiber of the system is connected to its previous neighbors, and in the matrix, this connection is given by

$$\begin{bmatrix}
& \vdots & \vdots & \vdots & \vdots & \vdots & \vdots & \vdots & \vdots & & \vdots & \vdots & \vdots & \vdots & \vdots & \vdots & \vdots & \vdots & \vdots & \vdots & \vdots & \vdots & \vdots & \vdots & \vdots & \vdots & \\
\cdots & 6 &&&&&&&& \cdots &&&&&&&&& -6 &&& -\beta_{ij} &&&& -1 & \cdots \\
\cdots & 6 & 2 &&&&&&& \cdots &&&&&&&&&& -2 &&&&&&& \cdots \\
\cdots & 3 & 2 & 1 &&&&&& \cdots &&&&&&&&&&& -1 &&&&&& \cdots \\
\cdots & 1 & 1 & 1 & 1 &&&&& \cdots &&&&&&&&&&&& -1 &&&&& \cdots \\
\cdots &&&&&&&&& \cdots &&&&& 6 &&&&&&&& -6 &&& 1 & \cdots \\
\cdots &&&&&&&&& \cdots &&&&& 6 & 2 &&&&&&&& -2 &&& \cdots \\
\cdots &&&&&&&&& \cdots &&&&& 3 & 2 & 1 &&&&&&&& -1 && \cdots \\
\cdots &&&&&&&&& \cdots &&&& 1 & 1 & 1 & 1 &&&&& -1 &&&&& \cdots \\
& \vdots & \vdots & \vdots & \vdots & \vdots & \vdots & \vdots & \vdots & \vdots & \vdots & \vdots & \vdots & \vdots & \vdots & \vdots & \vdots & \vdots & \vdots & \vdots & \vdots & \vdots & \vdots & \vdots & \vdots & \vdots & \ddots
\end{bmatrix}
\begin{bmatrix}
\vdots \\ a_{i-1,j} \\ b_{i-1,j} \\ c_{i-1,j} \\ d_{i-1,j} \\ e_{i-1,j} \\ f_{i-1,j} \\ g_{i-1,j} \\ \zeta_{i-1,j} \\ \vdots \\ a_{i,j-1} \\ b_{i,j-1} \\ c_{i,j-1} \\ d_{i,j-1} \\ e_{i,j-1} \\ f_{i,j-1} \\ g_{i,j-1} \\ \zeta_{i,j-1} \\ a_{ij} \\ b_{ij} \\ c_{ij} \\ d_{ij} \\ e_{ij} \\ f_{ij} \\ g_{ij} \\ \zeta_{ij} \\ \vdots
\end{bmatrix}
=
\begin{bmatrix}
\vdots \\ \alpha \\ \alpha/2 \\ \alpha/6 \\ \alpha/24 \\ \alpha \\ \alpha/2 \\ \alpha/6 \\ \alpha/24 \\ \vdots
\end{bmatrix}$$

System Boundaries

In order to tear the system apart from one side, the boundary at $x = 0$ was chosen to be free, meaning that there are no constraints on its slope or position. This provided a dangling tearable end. Apart from this, periodic boundaries were chosen in the y-direction, for simplicity. For the right boundary at $x = N_x - 1$, the boundaries were chosen such that the system could be thought of as infinite in the positive x-direction, mimicking the equilibrium height and slope of an intact system. This was done by fixing the height and forcing the slope to remain horizontal. This boundary will from here on be referred to as the *fixed boundary*. An illustration of the system boundaries can be seen in Figure 2.10. A mathematical description and the contribution to the system matrix will now be provided.

The solutions affected by the free boundary are $z^x_{i=0,j}$. A free end on the

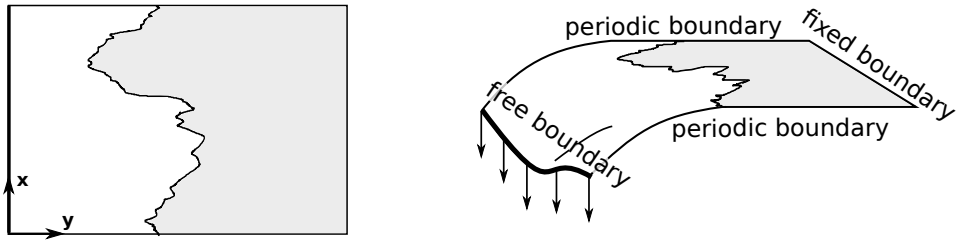

Figure 2.10: The boundary conditions chosen for this specific model. One end needs to be free in order to tear the system apart from one side. This end was chosen to be at $x = 0$. For simplicity, periodic boundaries were chosen for the y-direction and the remaining boundary at $x = N_x - 1$ was set to be fixed with a reasonable height and slope. When the deformations reach the fixed end, however, the boundary will affect the fracturing process and the result from this point on can not be used in the results.

beam simply means that it can have any height or slope, i.e. no constraints on $d_x z^x_{0j}(0)$ or $z^x_{0j}(0)$. However, point forces like $\beta_{i=0,j}$ and $\zeta_{i=0,j}$ are acting on the ends such that

$$d_x^3 z^x_{0j}(0) = -\beta_{0j} z^x_{0j}(0) - \zeta_{0j}. \tag{2.30a}$$

Because there is no forces acting on the beams lower than at $x = 0$, the beams experience no torques around this point, such that

$$d_x^2 z^x_{0j}(0) = 0. \tag{2.30b}$$

This takes care of the boundary conditions at $x = 0$.

For the fixed boundary at $x = N_x - 1$, the goal is that the system never "notices" that this boundary is fixed at all. This will not be true for the entire simulation, but for systems with low bending rigidity, this could be true for the majority of the simulation. Looking at the one-dimensional solution shown in Figure 2.6a, the height and slope of the beam at every intact fiber is given by $y_i(1) = -\alpha/\beta$ and $d_x y_i(1) = 0$. Because of the additional beam, this results in a height of $H = -2\alpha/\beta$ in two dimensions. It thus seem like a reasonable assumption to choose that

$$z^x_{N_x-1,j}(1) = -\frac{2\alpha}{\beta} \qquad\qquad d_x z^x_{N_x-1,j}(1) = 0. \tag{2.31}$$

Choosing these values, the boundary mimics the solution far into the intact region and the boundary conditions should only start affecting the solution at the time the deformations reach the fibers neighboring the fixed boundary. Now, inserting Eq. (2.25a) into Eqs. (2.30) and Eqs. (2.31) one finally gets

$$6a_{0j} + \beta_{0j}d_{0j} + \zeta_{0j} = 0 \tag{2.32a}$$
$$b_{0j} = 0. \tag{2.32b}$$

$$3a_{N_i-1,j} + 2b_{N_i-1,j} + c_{N_i-1,j} = \frac{\alpha}{6} \tag{2.32c}$$
$$a_{N_i-1,j} + b_{N_i-1,j} + c_{N_i-1,j} + d_{N_i-1,j} = \frac{\alpha}{24} + H. \tag{2.32d}$$

Taking into account Eqs. (2.29) which governs the internal fibers, the above expressions provides the required constraints needed to determine all the $8N$ unknowns of the free-fixed system.

System Load Parameter

In order to load the system in a way that tears it apart from one edge like indicated in Figure 2.10, the weight of the $i = 0$'th beam can be used as the driving force of the fracturing process. The weight of the loaded beam is denoted by α_L and is introduced by inserting it where α is given in Eq. (2.25b). α must therefore also be replaced with α_L in Eq. (2.29e) – Eq. (2.29h) as well, giving

$$z^y_{0j} = -\frac{\alpha_L}{24}y^4 + e_{0j}y^3 + f_{0j}y^2 + g_{0j}y + h_{0j}, \quad \forall\, j. \tag{2.33}$$

At the nodes along $i = 0$, the beams are connected through

$$6e_{0,j-1} - 6e_{0j} + \zeta_{0j} = \alpha_L \tag{2.34}$$
$$6e_{0,j-1} + 2f_{0,j-1} - 2f_{0j} = \frac{\alpha_L}{2} \tag{2.35}$$
$$3e_{0,j-1} + 2f_{0,j-1} + g_{0,j-1} - g_{0j} = \frac{\alpha_L}{6} \tag{2.36}$$
$$d_{0,j-1} + e_{0,j-1} + f_{0,j-1} + g_{0,j-1} - d_{0j} = \frac{\alpha_L}{24}. \tag{2.37}$$

Note that although α_L does not appear in the Eq. (2.25a) and Eq. (2.29a) – Eq. (2.29d), it does make an impact on the x-directed subsolutions through

the connecting force ζ_{ij}. It is also worth noting that there is nothing special about the load placement at $i = 0$ and it is just as straight forward to put it at any other location $i = x_L \neq 0$.

Breaking Criteria

If the mass of the beam mesh is neglected, i.e. $\alpha \approx 0$, the only load on the system is given through α_L and the right-hand-side (RHS) of the matrix equation, $\boldsymbol{b}$, now only contain nonzero elements linearly dependent on α_L. This means that given the load distribution, found by solving the matrix problem once for the given fiber configuration, the extension d_{ij} of the fiber increases linearly with α_L and the breaking criteria, Eq. (2.8), can be applied. To understand why, consider a change in the load by a factor μ, i.e. $\alpha_L' = \mu\alpha_L$. This gives

$$A\boldsymbol{x} = \mu\boldsymbol{b}'.$$

By in addition scaling the solution $\boldsymbol{x}' = \mu\boldsymbol{x}$ such that

$$\begin{aligned} A\mu\boldsymbol{x}' &= \mu\boldsymbol{b}' \\ A\boldsymbol{x}' &= \boldsymbol{b}', \end{aligned}$$

one can see that the solution $\boldsymbol{x}$ or, more specifically, the displacement of the ij'th node, d_{ij}, is increasing linearly with the load α_L. The linearity allows the problem to be solved *strain controlled*, and after finding the solution $\boldsymbol{x}$, the strain curve is obtained from the breaking criteria

$$\alpha_L' = \max_{i,j} \left\{ -\frac{d_{ij}}{t_{ij}} \right\} \alpha_L. \tag{2.38}$$

Here t_{ij} is the threshold of the ij'th fiber and the minus sign ensures that the fibers only can break downward direction.

Size Equals Stiffness

Analogous to the soft clamp model, the length scale determines the stiffness of the system [8, p.114]. The simplest explanation for this effect is to look at the bending rigidity B, which describes the stiffness of the system. Increasing B by a factor μ is equivalent to changing both β and α by a factor $1/\mu$, which is seen from Eq. (2.23). This means that the springs yield

more easily since β is now lower and the loading force done either through increased mass or gravity, must now be a factor of μ stronger in order to cause the same deformation as earlier. Therefore, one sees that decreasing both α and β effectively makes the system stiffer. However, α and β also depend on the lattice spacing a to the third power, meaning that changing a by a factor $\mu^{-1/3}$, gives exactly the same behavior as changing B.

2.3 FBMs and percolation

In the fracturing process of fiber bundles, the fibers will be in one of two possible states, intact or broken. A probability for the fiber to change state is governed by the threshold of the fiber. Such a system can be considered as a *percolation* problem. In percolation, one can have two or even more states that distribute themselves on a lattice according to a certain occupation probability. Every nearest-neighbor connected set of nodes with the same state forms a so-called *cluster*. When a cluster spans the entire size of the system by connecting two edges on opposite sides, the cluster is referred to as a *spanning cluster* Briefly explained, one could say that percolation is the study of such clusters. In the situation of the FBM studied here, only broken clusters is considered. The labeling of the clusters will be done using the Hoshen-Kopelman algorithm [20]. This procedure is explained in detail in Appendix B.1.

Another thing worth mentioning is *gradient percolation*, where one introduce a gradient $g = 1/N_x$ in the occupation probability $p(j) = gj$ of node j [21]. In the light of FBM, this may be physically interpreted as a stiff clamp being pulled at an angle instead of straight down, like for ELS. This is illustrated in Figure 2.11.

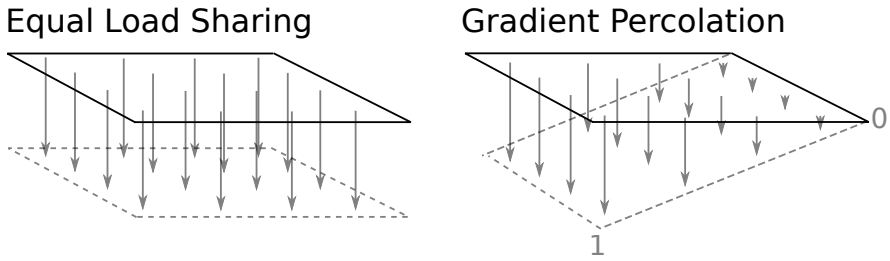

Figure 2.11: Physical interpretation of ELS versus gradient percolation. Gradient percolation can somehow be considered as an ELS FBM with a gradient in either the force or the theshold value, giving a tilted pull.

2.4 Fracture Front Morphology

By studying the geometry of the fracture front, one can see that it looks differently on different length scales. By investigating this scaling behavior, an indication of the underlying processes that drive the fracture may be found. This section is meant to provide the reader with the required background and terminology to understand why this is the case. With this out of the way, Section 2.4.3 will give quantitative description of the experimental results that will be used for comparison with the simulated results of the thin plate Bridge Model.

2.4.1 Fractals

In 1984, Mandelbrot said that the rough and irregular surface left behind after a fracturing process could be considered to be fractal [4]. But what is a fractal? In short, one could say that a fractal is an object with surface structures that depends on the resolution used to study it. Even if one could endlessly magnify its surface, the details would never flatten out but simply continue for infinity. In fact, fractals tend to repeat their structure at many length scales. One says that they are *self-similar*. Another curiosity about this kind of behavior, is that fractals have scale dependent length, which goes to infinity as the resolution increases. Both these properties can easily be seen from the fractal Koch curve shown in Figure 2.12. In fact, there are

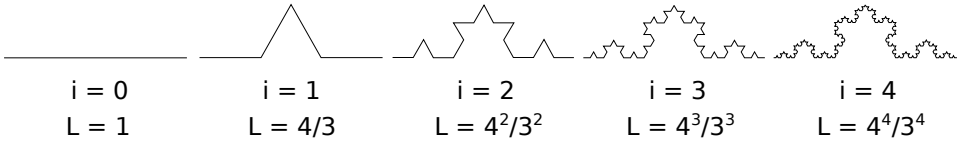

Figure 2.12: The first iterations, of a Koch curve with the corresponding length L of the segment. The Koch curve is a true fractal with infinite length and self-similarity. The latter property can be seen by noting that the first third of the curve at any iteration is identical to the entire curve of the previous iteration, only scaled down to 1/3 of the size. The figure is adapted from [3].

many natural occurring phenomenons that exhibit fractal properties. Just go to the grocery store and study a cauliflower or look at the coastlines on a map [22]. Even in cosmology, it can be encountered in the distribution of galaxy clusters [23].

2.4.2 Fractality of Fracture Surfaces Explained Through Coastlines

One can somehow consider the morphology of fracture surfaces be similar to that of geographical coastlines. In 1967, Mandelbrot described coastlines as having a fractal nature by showing statistical self-similarity and lack of a well defined length [22]. The latter is illustrated in Figure 2.13. [1]. If one

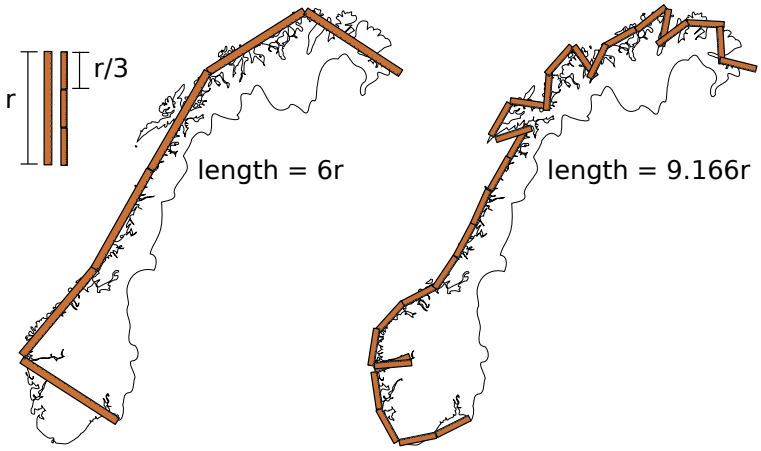

Figure 2.13: A ruler of length r is used to measure the coastline of Norway through compass walk. By reducing the size of the ruler, the measured length l between points increases, i.e. it depends on the length of the ruler.

wants to measure the length of a coastline, or similarly; a fractured surface, one could lay out n equally sized rulers of length r, through compass walk, until the entire length of a coast is transversed, as shown in Figure 2.13. The number of rulers gives an estimate of the coasts length by using $l = nr$. If the coast is self-similar, then the required number of rulers needed to transverse the coast should follow

$$n = Cr^{-D_f}, \tag{2.39}$$

[1] As mentioned in Mandelbrot's paper [22] the west coast of Britain was selected as an extreme example of a natural fractal due to its highly irregular coastline, resulting in fractal dimension $D_f = 1.25$. However, the coastline of Norway shows a fractal dimension of $D_f = 1.52$ [24, p.8][25, p.22].

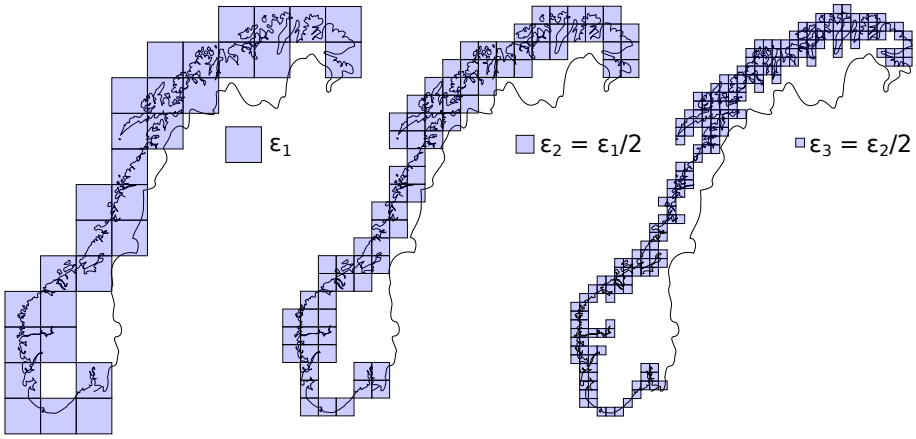

Figure 2.14: The box-dimension of the coast of Norway if found by comparing the number of boxes needed to cover the coastline for different grid spacings, giving the size of the boxes.

where C is some constant. By either rewriting Eq. (2.39), or using n boxes of size $\epsilon \to 0$ as illustrated in Figure 2.14 [26], an expression for the quantity D_f is obtained,

$$D_{f,c} = \frac{\log n}{\log \frac{1}{r}} \qquad\qquad D_{f,box} = \lim_{\epsilon \to 0} \frac{\log n(\epsilon)}{\log \frac{1}{\epsilon}}. \tag{2.40}$$

This quantity is known as the *fractal dimension* and gives a more general description of the length of the curve. If one knows the fractal dimension, one can simply estimate the length at any scale using Eq. (2.39) [27][25, p.22]. The fractal dimension is a non-integer number that can be viewed as an extension of the integer dimensions: a line with $D_f = 1.05$ is similar to a straight 1D line, while a line with $D_f = 1.95$ curls and wiggles so much that it fills space much like a surface. As an example, the Koch curve shown in Figure 2.12 has a fractal dimension of $D_f = \log 4 / \log 3 \approx 1.2619$.

2.4.3 Self-affinity and the Roughness Exponent

A property closely related to self-similarity, is *self-affinity*. If self-similarity is invariance under isotropic magnification, then self-affinity is invariance under anisotropic magnification. This means that if the geometry of the

fracture front $G(x)$ is self-affine, then shrinking the x-axis by a factor $1/\mu$ and rescaling the height of front by a factor $\mu^{-\zeta}$ will leave it unchanged, i.e. [28, p.5]

$$G(x) = \mu^{-\zeta} G(\mu x). \tag{2.41}$$

The exponent ζ is called the *roughness exponent* or Hurst exponent [29]. For fractured surfaces which are only statistically self-affine, Eq. (2.41) is only valid in a stochastic sense. Using the probability density for finding the crack at height G at position x, Eq. (2.41) can be extended to [3]

$$p(G, x) = \mu^{-\zeta} p(\mu^{\zeta} G, \mu x). \tag{2.42}$$

ζ is an example of a *critical exponent*. Critical exponents are used to describe physical quantities near phase transitions. A quantity described by a critical exponent will follow a *power law* in the vicinity of the phase transition, and typically indicates that the process is resulting from a characteristic underlying mechanism. Quantities from completely different systems can end up having the same critical exponents, following the same power law distribution. The critical exponents are in this way *universal* and systems that have the same critical exponents are said to belong to the same *universality class*. [30, 31] As will be explained in the next section, the morphology of the fracture front seen experimentally gave rise to two different scaling behaviors in the form of roughness exponents, indicating that there could be two different mechanisms driving the process.

2.4.4 Historical background and Experimental Results

Using the experimental setup of Schmittbuhl and Måløy, first introduced in 1997, Santucci et al. [7] managed to measure one small small scale roughness exponent , $\zeta_{small} = 0.60 \pm 0.05$, consistent with the one Schmittbuhl and Måløy had found earlier in addition to a large scale exponent of $\zeta_{large} = 0.35 \pm 0.05$. This was the first time anyone had measured two different exponents in the same experiment. This gave rise to the idea that there could be two different fracture mechanisms at work on different length scales [32]. The large scale behavior is consistent with the earlier model of Schmittbuhl et al. [33], treating the front as a fluctuating elastic

line passing through the material. The small scale behavior on the other hand was thought to be caused by coalescence of voids located ahead of the front [32, 11], and is consistent with the scaling behavior $\zeta = 2/3$ of a front driven by gradient percolation [21, 34].

A dynamical study, related to the distribution of velocities in the crack propagation, was also conducted using the experimental setup of Schmittbuhl and Måløy. This was conducted by Tallakstad et al. [6], who found that the velocity distribution of the front followed a power law

$$p\big(v/\langle v\rangle\big) \sim \left(\frac{v}{\langle v\rangle}\right)^{-\eta}, \quad for \quad \frac{v}{\langle v\rangle} > 1, \tag{2.43}$$

in the depinning regime, with $\eta = 2.55 \pm 0.15$ [6]. Here v is the local velocity of the front, $\langle v\rangle$ is the global average velocity. The pinning regime is the referred to as the region where the front is slowed down, i.e. $v < \langle v\rangle$, and the depinning regime, $v > \langle v\rangle$, is where it moves fast.

Inspired by the work of Gjerden [3], who managed to reproduce these experimental values using the thick plate SCFBM, this thesis tries to do the same by using the thin plate Bridge Model. The theory used for estimating the roughness exponent ζ, based on the morphology of the front, will be presented in the following section. However, one first needs to obtain the geometry of the front. This will be explained in Chapter 3, where the algorithms, used to obtain both the morphological and dynamical structure of the front, will be explained more carefully.

2.4.5 Estimating the Roughness exponent

When a fracture front has stabilized, its width $w_{f,S}$ is assumed to follow a power law with system size to the power of the roughness exponent

$$w_{f,S} \sim {N_y}^{\zeta}. \tag{2.44}$$

The time it takes before the front stabilizes is called the *saturation time* and also tend to follow a power law with increasing system size. Because the system is solved quasi-statically, there is no explicit time. Using the number of broken fibers k as the clock of the system, the saturation time k_S

should follow

$$k_S \sim {N_y}^Z, \tag{2.45}$$

where Z is called the *dynamic exponent* [35, p.23]. Because k is used as the clock of the system, the breaking rate of the fibers is constant, and one can assume that the average position of the front follows [35, 20]

$$x_f \sim k, \tag{2.46}$$

such that the scaling relation for k also hold for x_f. If all the above relations hold, one should be able to use Family-Vicsek scaling [28] in order to remove the L-dependence of both x_f and w_f. Family-Vicsek scaling assumes that

$$w_f(N_y, x_f) = w_{f,S}\, \rho\left(\frac{x_f}{x_{f,S}}\right), \tag{2.47}$$

where

$$\rho(x) = \begin{cases} x^b & \text{for } x \ll 1 \\ \text{constant} & \text{for } x \gg 1, \end{cases} \tag{2.48}$$

Here b is the so-called *growth exponent* [35, p.22] and $x_{f,S}$ is the position corresponding to k_S. Because the correlation length early on in the system is much smaller than the total size of the system, finite size effects are negligible, leading to

$$w(N_y, x_f) \sim {N_y}^\zeta \left(x_f {N_y}^{-Z}\right)^b = \underbrace{{N_y}^{\zeta - Zb}}_{\sim 1} x_f^b \sim x_f^b \tag{2.49}$$

and

$$b = \frac{\zeta}{Z}. \tag{2.50}$$

Assuming Eq. (2.44), Eq. (2.45) and Eq. (2.46) hold, the dependence of the width, N_y, can be rescaled away, giving only a one parameter description of $w_f(x_f)$.

Chapter 3

Methods and Algorithms

3.1 Random number generator

The random numbers generated for numerical simulations were obtained using the xorshift1024* Random Number Generator (RNG) [36], which is reviewed as an excellent general-purpose, high speed pseudo RNG [37]. With a period of $(2^{1024} - 1)$ it was regarded as sufficient for the relatively small systems simulated in this thesis. For reproducibility, the seeds used in every simulation have been stored along with the parameters of the system.

3.2 Solving the matrix problem

The final matrix shown in Figure 3.1 is a $8N \times 8N$ sparse non-symmetric matrix with a number of $(31N_xN_y - 5N_y)$ non-zero elements. The matrix is also not positive-definite. However, because the elements of the matrix is known, it can be made implicit avoiding the trouble and memory use of storing all its elements. Such a solver was made using conjugate gradient (CG) on the normal equation $A^TAx = y$ and $AA^Tx = y$. AA^T and A^TA are both symmetric positive-definite and the solution should therefore convergence. However, the convergence of the algorithm gets worse as the number of broken fibers k increases. Because of this, the CG method was replaced with the sparse solver `sp_solve()` of armadillo [38]. With this, a computational speed sufficient to solve $N = 50^2$ systems was acquired.

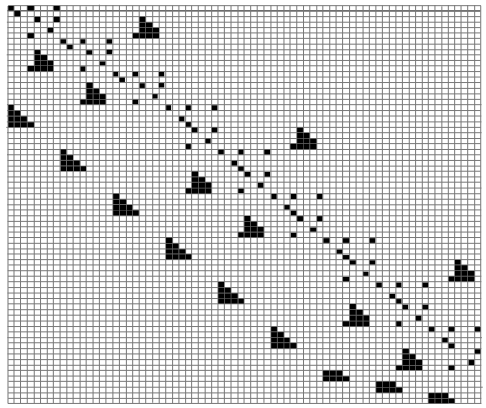

Figure 3.1: Illustration of the 264 non-zero elements of the 72×72 matrix resulting from a system of $N = 3^2$ fibers. The non-zero elements are shown as black pixels.

Armadillo also provides sparse containers, such that one only needs to store the $(31N_xN_y - 5N_y)$ non-zero elements.

3.2.1 Window solver

It should be emphasized that the main bottle neck of this problem is solving the matrix. The matrix has no apparent positive qualities except for being sparse. Increasing the number of fibers in the system, N, increases both the time spent solving the $8N \times 8N$ matrix at every iteration in addition to the total number of iterations required to rupture the entire bundle, given by N. Another problem when simulating the model, is that the front requires time to reach a stable geometry. This together with the effects of boundary conditions at the end of every simulation, gives a sampling region of about 20-30 % for the equilibrium stage. This however depend greatly on the stiffness of the system, which governs the range of interaction. Inspired by the conveyor belt technique of Gjerden [3], it was attempted to create a solution window moving over a longer system of intact fibers, possible due to the directionality and the very localised fracturing zone, illustrated in Figure 3.2. The size of the fracturing zone will depend on the stiffness of the system. For soft enough systems, the interaction lengths of the model should be so small that a window of relatively small size should be able to contain the entirety of the deformed region.

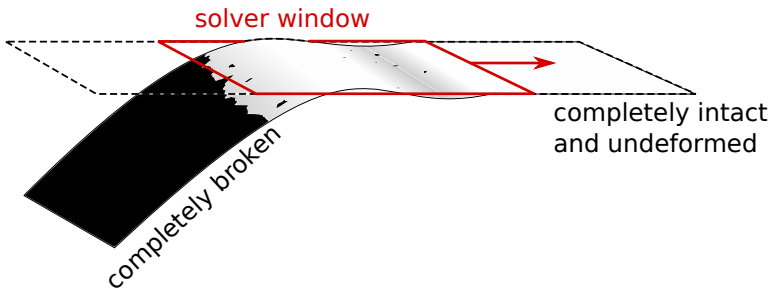

Figure 3.2: Due to the directionality, the presumably finite interaction length and the localised fracturing zone, it should be possible to solve the system only in a small window stretching from the completely broken region to the undeformed intact region. The conditions at right boundary of the system, Eqs. (2.31), were chosen for this reason, assuming to be far within the intact region.

Movable load

In order to cut away the region of completely broken fibers, the load would need to be moved after the front for the system to be loaded.. Lacking the time to do a proper statistical analysis of both scenarios, it was required that the movable load had to give the same fracturing sequence of fibers as the stationary load to assure consistency with the fixed end load used in the experimental setup [5]. This did not turn out to be the case and the movable load was not further investigated. This is more thoroughly explained in Appendix C.

The next best approach would be to have a solver window with increasing size, fixed to the left end of the system at $x = 0$. This approach will not remove the clamp beneath broken fibers, as they are required to correctly include the force propagation from $x = 0$ to the fracture zone. This was however not achieved during the limited time of this work and the presented results are therefore only based on a solver solving for the entirety of the system.

3.3 The FBM fracture front

Before the fractal geometry of the front can be evaluated, it first needs to be defined and located. The front is found from the sequence of breaking fibers. Each time a fiber breaks, the arising cluster is labeled using the

Hoshen-Kopelman algorithm [20]. The broken cluster(s) bordering the left boundary of the system is set to constitute a larger cluster which here will be referred to as the *void cluster*. This cluster could also be referred to as the *infinite cluster* of the broken state [39]. When the void cluster is found and labeled, the front is then located just by moving along the connected broken-intact interface. A detailed description of this method is is given in Appendix B.
How the front is located depends on how it is defined, which can be done in numerous ways. The simplest definition would be the intact *reduced front*, defined as the first encountered intact fiber bordering the void cluster, when running right-to-left, for every row. To be on the safe side, a more detailed description, closer to the actual continuous broken-intact interface, will be used. At the interface where the void cluster and the infinite intact cluster meet, the set of bordering broken fibers, connected together by nearest-neighbor contact, constitute the *broken front*. On the other side, the *intact front* will be defined as every intact fiber which is nearest-neighbor to the broken front.The intact and broken fronts are illustrated in Figure 3.3. The definitions of these percolation fronts are inspired by [17, 39, 40].

Because the actual front of the system is the interface between the void cluster and the intact cluster, the definition of the front is chosen to be the weighted average between the broken- and the intact fronts [39]

$$x_f = \frac{x_{if} n_{if} + x_{bf} n_{bf}}{n_{if} + n_{bf}}. \tag{3.1}$$

Here, n_{if} and x_{if} is the number of intact nearest neighbors of the void cluster and their average position, respectively. Likewise is n_{bf} the number of broken neighboring fibers to the intact cluster and x_{bf} the average position. The width of the intact and broken fronts, w_{if} and w_{bf}, are defined as the standard deviation of the position of their constituent fibers. Followingly, the width of the wheighted front is therefore given by

$$w_f^2 = \frac{w_{if}^2 n_{if} + w_{bf}^2 n_{bf}}{n_{if} + n_{bf}}. \tag{3.2}$$

Because the width of the intact and broken front should behave similarly [39], a simpler definition such as $w_f = w_{if}/2 + w_{bf}/2$ could perhaps also have been used. This will be tested in order to verify the that the choice of

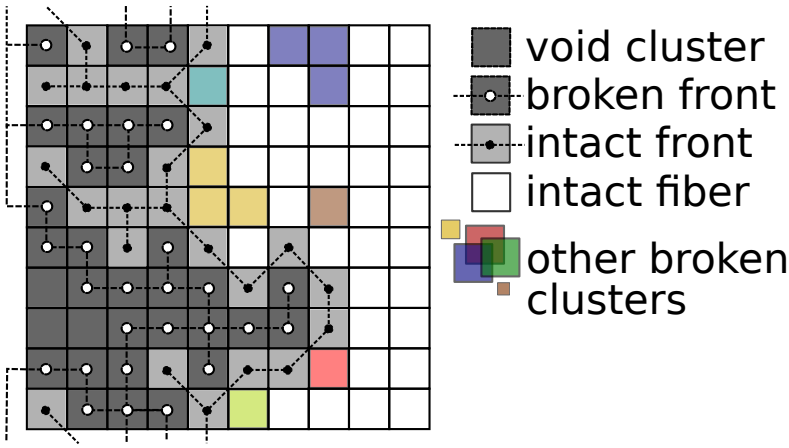

Figure 3.3: The definitions of the intact and broken fronts. The void cluster is constructed from all clusters bordering the left boundary of the system. The figure is adapted from [17, 39].

definitions is reasonable.

Lastly, the length scaling properties of the front will be defined through the box counting dimension, Eq. (2.40), choosing the size of the boxes equal to the size of the pixels representing the fibers. The fractal dimension of the intact and broken front is therefore given by

$$D_{if} = \frac{\log n_{if}}{\log N_y} \qquad D_{bf} = \frac{\log n_{bf}}{\log N_y}, \tag{3.3}$$

3.4 Front velocity and the waiting time matrix technique

In order to calculate the velocity of the fracture fronts and obtain the velocity distribution, the waiting time matrix (WTM) method [41, 6] have been used. It should be noted that there is no explicit time in this model, as it is solved quasi-statically. The only thing that changes is the number of broken fibers, k, and will be used as the measurement of time. The WTM technique can be understood by imagining the front, the broken or the in-

tact, moving over the system. Every fiber, or pixel, has a number assigned to it and is represented by a matrix. At every time step, all the matrix cells which are currently a part of the front are incremented by one. Initially all these numbers are set to zero. But after the front has passed the elements during the evolution of the system, the pixels contain numbers corresponding to how long time the front has been on top of them. These numbers, or waiting times, constitute the WTM. An illustration of this is given in Figure 3.4. In this way, low valued elements of the WTM represent that the front

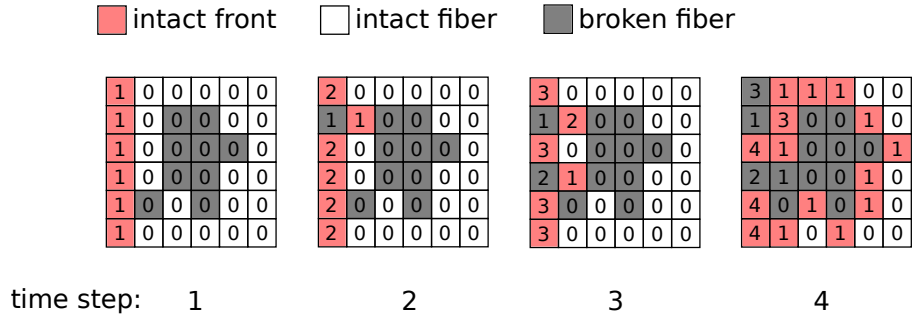

Figure 3.4: A toy example that demonstrates how the waiting time matrix (WTM) is obtained from the intact moving front. The position of the front is shown in red. The WTM for the broken front is found equivalently, but the front looks different as it is constrained to nearest-neighbor connections, see Figure 3.3.

has moved quickly across them, while high valued elements represent that the front has remained there over several time steps, either pinned down or moving slowly. In fact, by inverting each element of the WTM one obtains the spatiotemporal map of velocities v_{ij} of the front, giving high velocities for low waiting times, and low velocities for large waiting times. The zero valued elements of the WTM resulting from coalescence, meaning that the front merges with a void ahead of the front, give infinitely large velocities and are not included in the sampling of the velocity distribution.

3.5 Choice of parameters

As discussed in the last part of Section 2.2.2, the large scale and the small scale behavior or the fracture front can be investigated by varying β, meaning that the clamp acts stiffer on small scales than on large scales. However, when β approaches zero, the length of interaction increases. In order to keep the interaction with the fixed boundary to a minimum, test simulations for a 100×10 system was made to see how far the deformation of the clamp stretches for different β. Based on this, it was decided that only a small range of β values could be investigated without a large contribution from the boundary of the system. This will be presented in the following Chapter along with the results.

3.6 Last Minute Change: The Hinged Bridge model

Halfway into the simulation process, while trying to reproduce the small scale behavior of the thin plate, it was realised that the fixed boundary conditions was not as good of a choice as first presumed. Realising that the ELS or percolation type behavior, typical for stiff systems, would perhaps only be obtained if the model managed to stretch itself out, and become flat. This seemed not to be obtainable with the horizontally fixed boundary as illustrated in Figure 3.5. In order to obtain a system that could be allowed

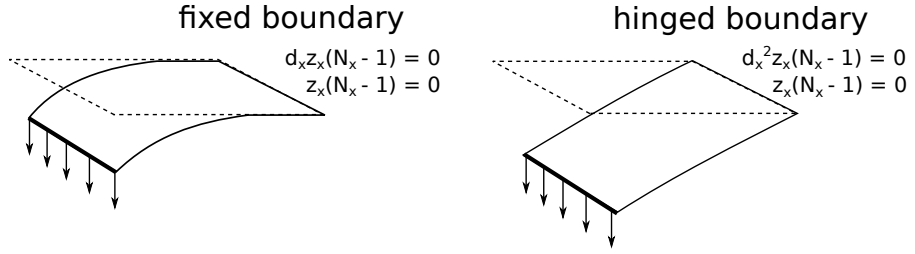

Figure 3.5: The horisontally fixed Bridge Model versus the Hinged Bridge Model. The fixed model never seems to be able to straighten out, even for $\beta \to 0$.

to stretch out for small values of β, the current fixed boundary was replaced

by a hinged boundary

$$z^x_{N_x-1,l}(1) = 0 \qquad\qquad d_x^2 z^x_{N_x-1,l}(1) = 0, \tag{3.4}$$

giving

$$a_{N_x-1,l} + b_{N_x-1,l} + c_{N_x-1,l} + d_{N_x-1,l} = \frac{\alpha}{24} \tag{3.5}$$

$$6a_{N_x-1,l} + 2b_{N_x-1,l} = \frac{\alpha}{2}. \tag{3.6}$$

With these boundary conditions, the number of elements in the matrix is now $(31N_xN_y - 6N_y)$. In addition, for $k/N \sim 1$ the angle of the solution becomes so steep that the matrix becomes singular. This was quick-fixed by using the solution for $k = (N - N_y)$ for the last N_y iterations. This assumption is believed to be adequate, regarding both to the stiffness and linearity in the extension of the fibers. The model with the new boundaries will here be referred to as the Hinged Bridge model. More on why the hinged boundary conditions are more reasonable than the fixed boundary conditions will be given in Chapter 5.

Chapter 4

Results

4.1 Test simulations

Based on the deformations for the $N_x \times N_y = 100 \times 10$ system shown in Figure 4.1, it was decided that $\beta = 10^{-4}$ would result in so long range interactions that the fixed boundary at $x = N_x - 1$ would interfere noticably with the fracture front for a system of length $N_x = 50$. To verify this assumption, simulations for $\beta = 10^{-4}$ were also conducted.

As the last test, Figure 4.2 shows the evolution for the different definitions of both the position and the width of the front.

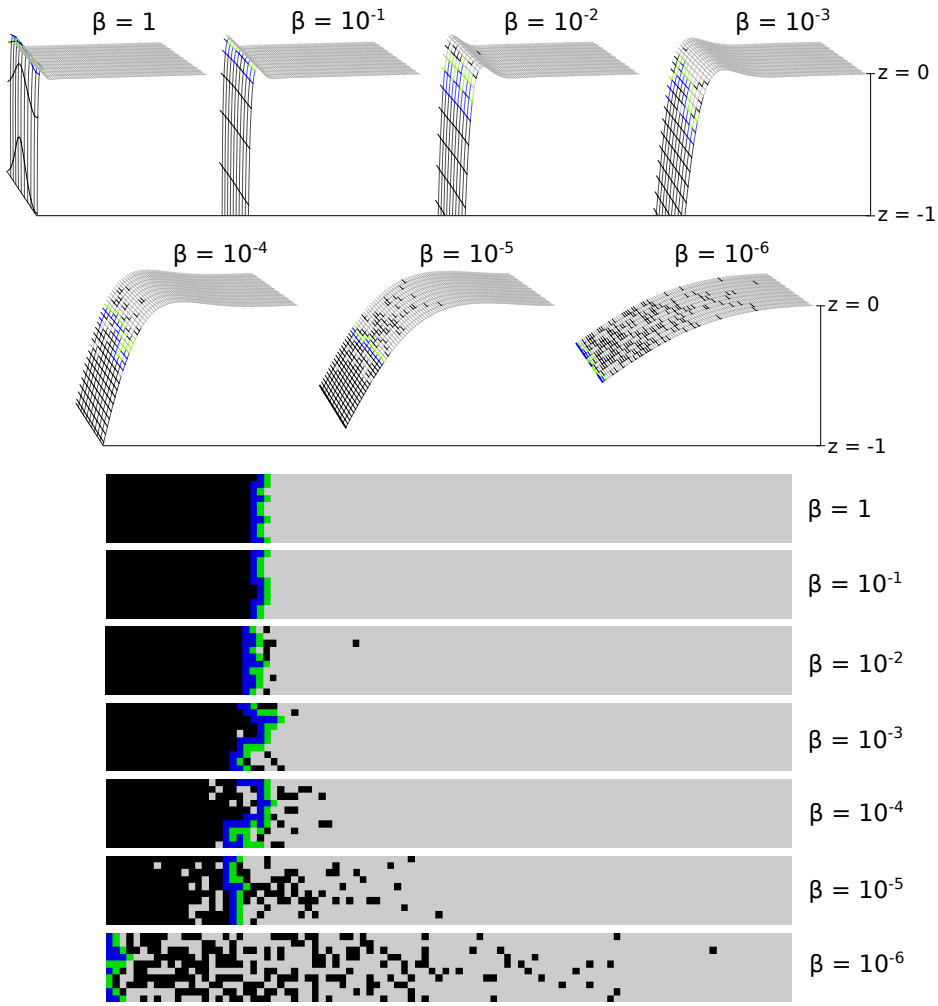

Figure 4.1: A clear deformation bumb for a 100x10 system at $k/N = 0.2$. The reach of the deformation into the system increaes with β and seems to disappear at $\beta = 10^{-6}$. The shape of the bump is belived to result from the beams resistance to bending and because it cannot have a discontinuity in its slope. The corresponding 2D pixel representation of the fibers is shown below. Fibers that are broken, part of the broken front, part of the intact front or simply just intact, are represented by black, blue, green and grey, respectively.

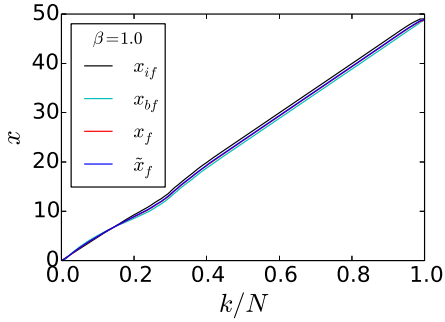

(a) front position

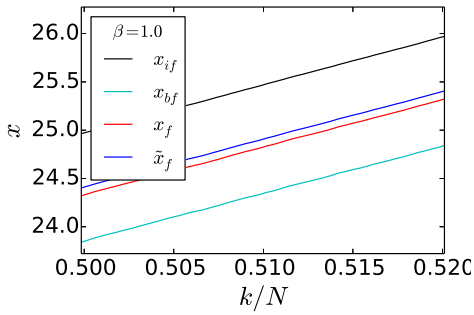

(b) front position (magnified)

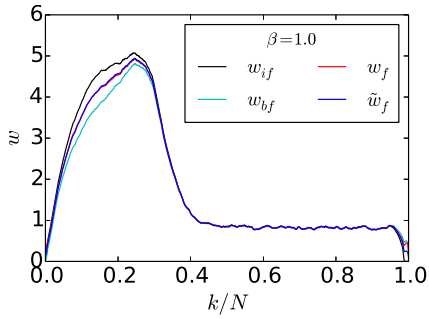

(c) front width

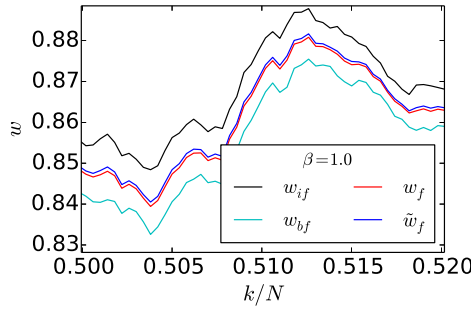

(d) front width (magnified)

Figure 4.2: **(a)** and **(b)** shows the average front position for the intact front x_{if}, the broken front x_{bf}, the average front $\tilde{x}_f = (x_{if} + x_{bf})/2$ and the weighted front x_f for $\beta = 1$. x_f is closer to x_{bf} due to the additional length of the broken front caused by the nearest neighbor connection. The same is seen for the widths shown in **(c)** and **(d)**.

4.2 Fixed Boundary Conditions

This section provides the results obtained by using the horizontally fixed boundary conditions, given by Eqs. (2.31). The number of instances run for the different system parameters is shown in Table 4.1. The system length N_x is kept fixed, but the width N_y will be used as a variable.

Figure 4.5 shows some threshold velocity maps $V_{C,bf}$ [6] for the broken front with $\beta = 1$. In the depinning regime, the threshold maps are defined

Table 4.1: The number of samples simulated the different values of β and system sizes $N_x \times N_y = 50 \times N_y$. The average quantities presented in this section is averaged over the given number of samples.

N_y	$\beta = 1$	$\beta = 10^{-1}$	$\beta = 10^{-2}$	$\beta = 10^{-3}$	$\beta = 10^{-4}$
10	101	-	-	100	100
20	100	-	-	100	105
30	100	-	-	100	63
40	101	-	-	100	60
50	104	116	100	150	52
60	40	-	-	-	30

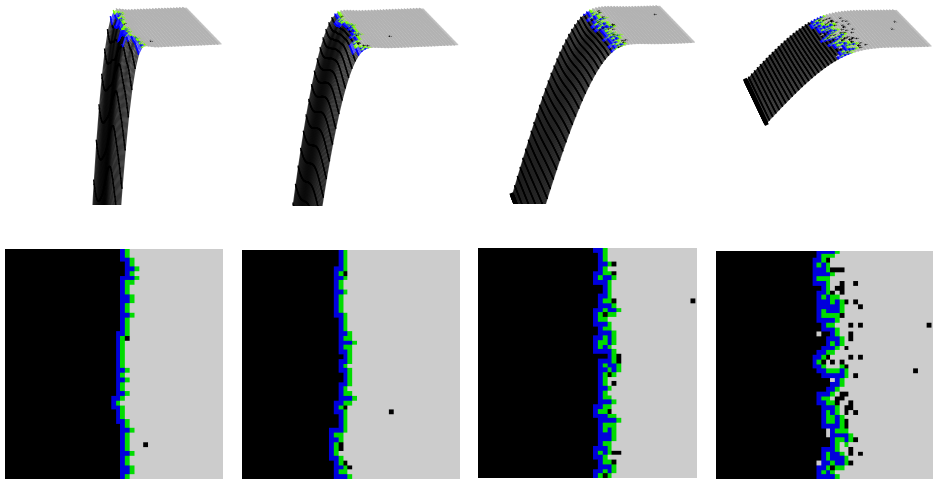

(a) $\beta = 1$ **(b)** $\beta = 10^{-1}$ **(c)** $\beta = 10^{-2}$ **(d)** $\beta = 10^{-3}$

Figure 4.3: Snapshots of the geometry of a 50×50 system for different values of β. The snapshot shows the 3D shape (top) with the corresponding configuration of fibers (bottom). The colors representation is the same as in Figure 4.1.

such that

$$V_{C,bf} = \begin{cases} 1, & \text{for } v_{bf} \geq C\langle v_{bf} \rangle \\ 0, & \text{for } v_{bf} < C\langle v_{bf} \rangle. \end{cases} \tag{4.1}$$

This way, the regions were the front moves relatively fast is shown as white regions. The regions that survive with increasing C, represent even faster

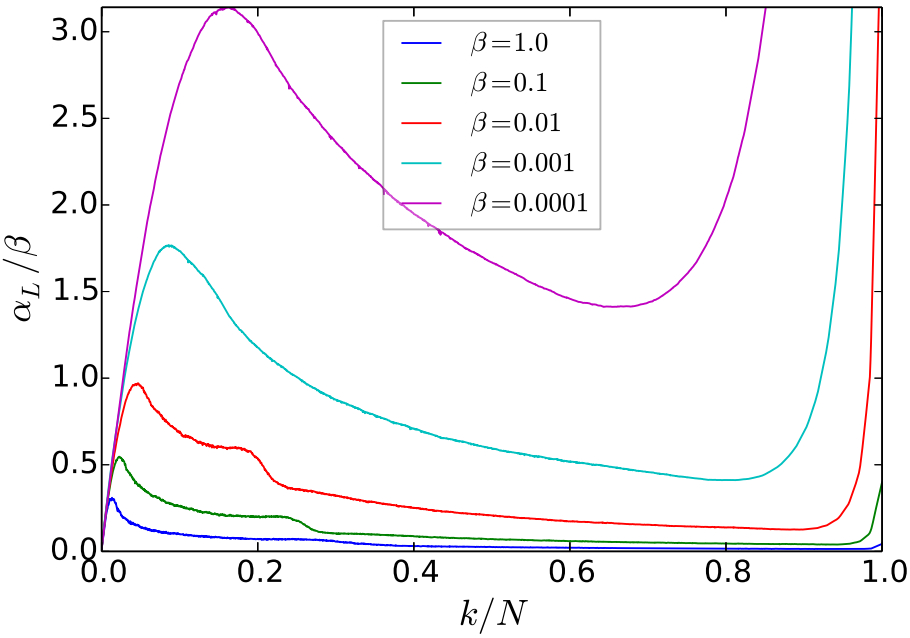

Figure 4.4: The applied load α_L required to break the k'th fiber. The load is rescaled by β to make the curves comparable.

movement. Similarly, the pinning regions are shown by defining

$$V_{C,bf} = \begin{cases} 1, & \text{for } v_{bf} \leq \langle v_{bf} \rangle / C \\ 0, & \text{for } v_{bf} > \langle v_{bf} \rangle / C. \end{cases} \tag{4.2}$$

For the pinning velocity maps, the white regions now give where the front is pinned down, and larger C give even larger pinning.

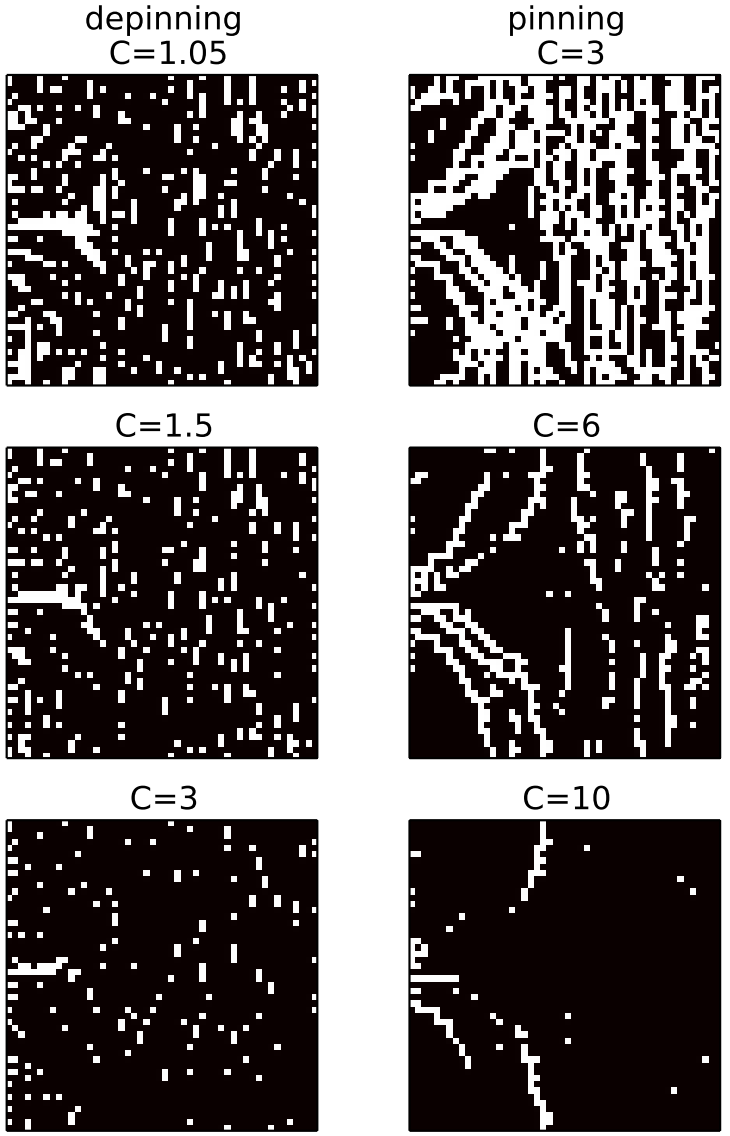

Figure 4.5: The threshold velocity map $V_{C,bf}$ of the broken front for $\beta = 1$. In the depinning regime, white regions represent velocities larger than $C\langle v_{C,bf}\rangle$. In the pinning regime however, white regions represent velocities lower than $\langle v_{C,bf}\rangle/C$

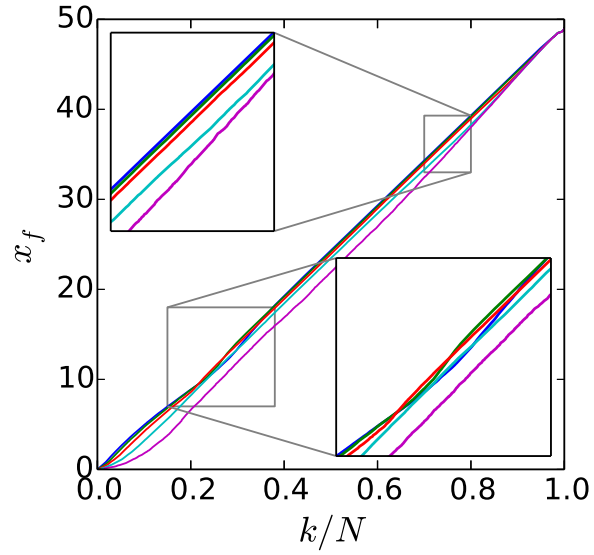

(a) average front position

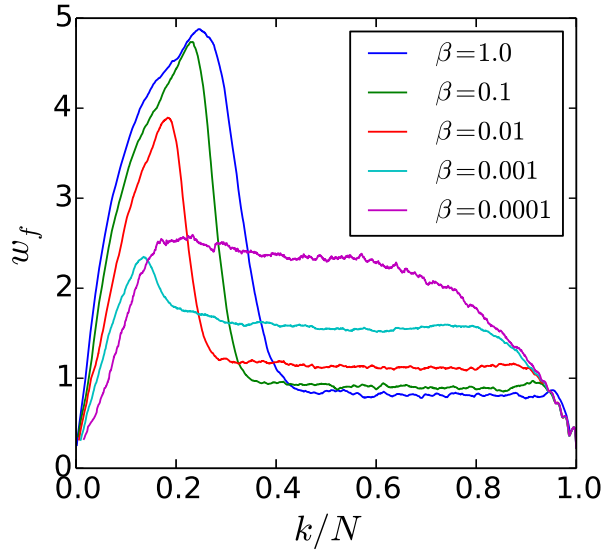

(b) average front width

Figure 4.6: The average front position **(a)** and average front width **(b)**, for $N = 50^2$. The upper inset in **(a)** shows the general stable behavior through the simulations, except for $\beta = 10^{-4}$ which reaches stability earlier.

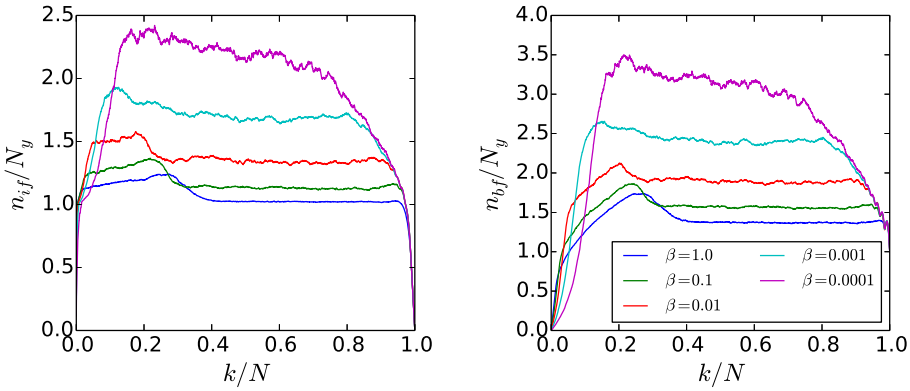

(a) length of the intact front **(b)** length of the broken front

Figure 4.7: The average front lengths for $N = 50^2$.

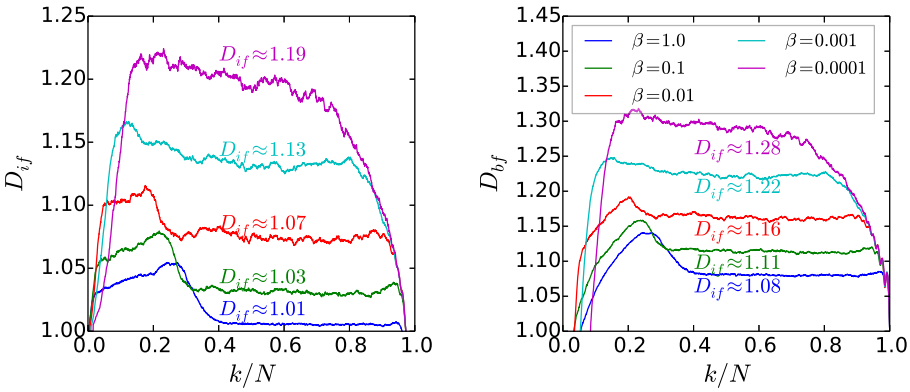

(a) **(b)**

Figure 4.8: The resulting fractal dimension for both the intact **(a)** and broken front **(b)** for $N = 50^2$.

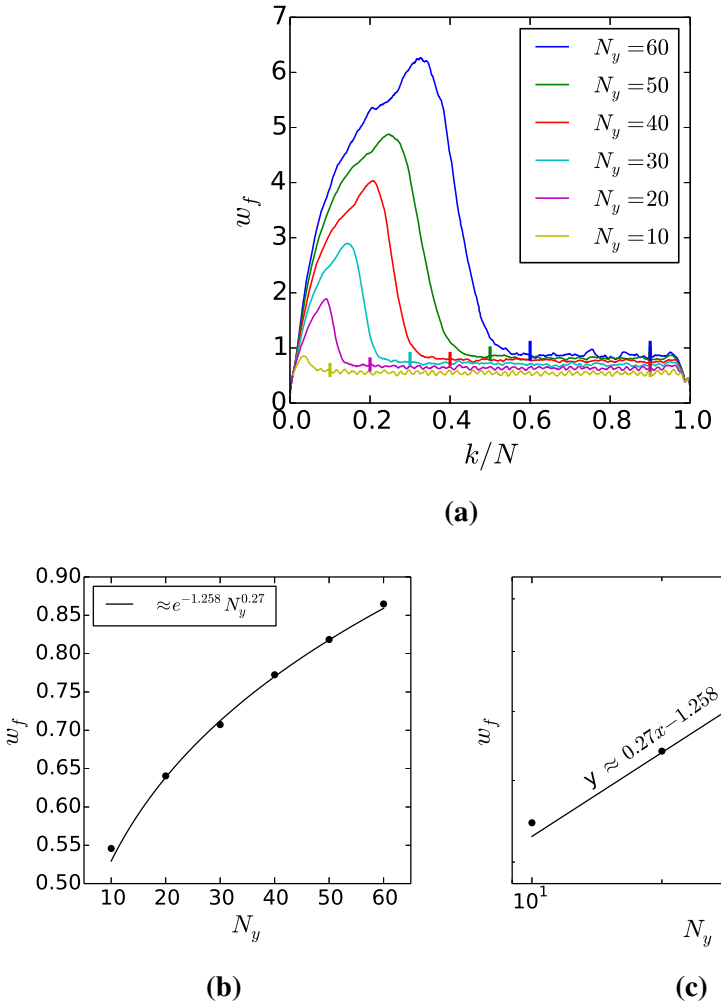

Figure 4.9: The front width as a function of the width of the system for $\beta = 1$. **(a)** shows the evolution of the width w_f for different system sizes $N_x \times N_y$. The stable region of the width is then sampled, marked by the vertical ticks and give the behavior shown in **(b)** and as log-log plot in **(c)**. The points show consistency with a possible power law. This was also done for the widths of the intact and broken fronts, resulting in fitting slopes of ≈ 0.278 and ≈ 0.264, respectively. Appart from the slopes, the shape in log-log space was visibly the same. Due to the fairly few samples considered, the roughness exponent is estimated to $\zeta \approx 0.27 \pm 0.06$.

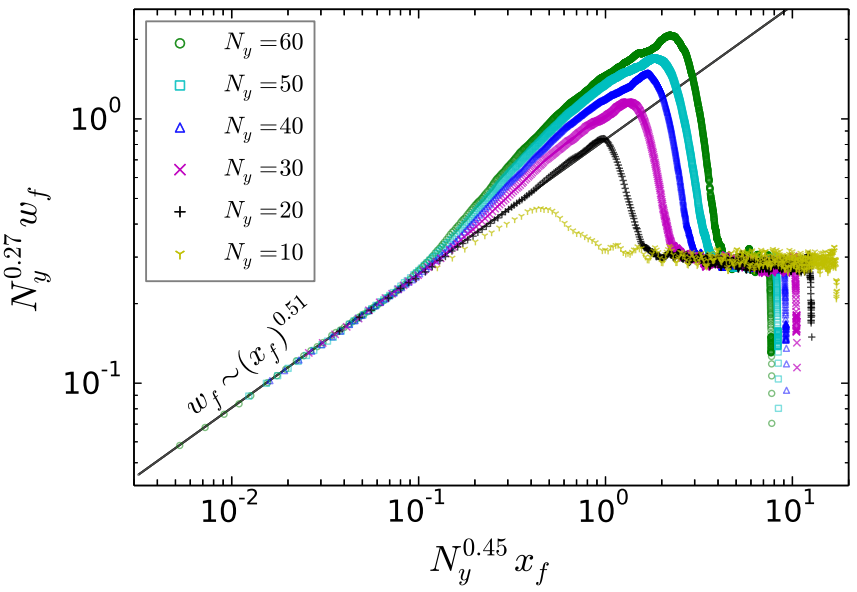

Figure 4.10: The front width as a function of the front position with Family-Vicsek scaling, $N_y^{\zeta} w_f(N_y^Z x_f)$, showing data collapse for both the early formation and stable region of the front. Data collapse for the stable region was obtained using the slope in Figure 4.9c, which gives the roughness exponent estimate. Given the data collapse in the y-direction, a dynamic exponent of $Z \approx 0.45 \pm 0.09$gave the best data collapse for for small x_f, The slope of the growth region, based on the data points, were estimated to $\approx 0.51 \pm 0.04$. However, due to the insecurities in the averaged data, the estimation of the growth exponent was rounded up to $b \approx 0.5 \pm 0.1$.

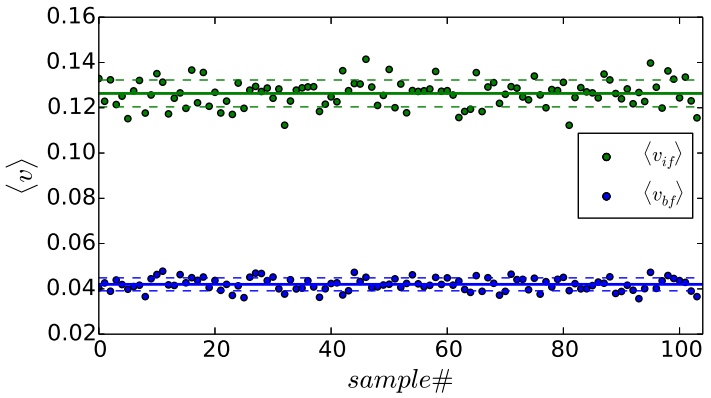

Figure 4.11: The variations of the intact and broken global velocities, $\langle v_{if} \rangle$ and $\langle v_{bf} \rangle$ for the 104 samples of the $50x50$ system of $\beta = 1$. The solid and dashed lines give the mean and standard deviation, respectively.

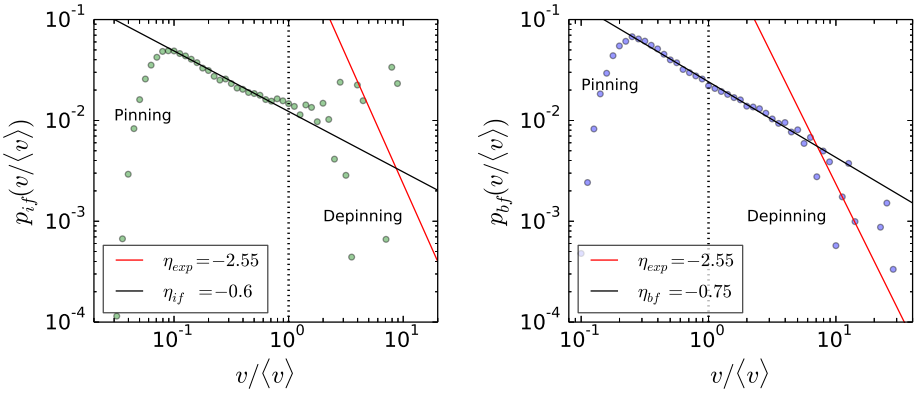

(a) **(b)**

Figure 4.12: The velocity distribution for the intact **(a)** and the broken front **(b)** of a soft 50×50 system with $\beta = 1$. The distrubution was obtained by using logarithmic binning, and the variations shown in Figure 5.4 have also been taken into account. In the transition between the pinning and depinning regime, a power-law-like behavior is seen for the broken front, with a slope of approximately $\eta_{bf} \approx 0.75 \pm 0.07$. Trying a fit to the intact front as well, yields a slope of $\eta_{if} \approx 0.6 \pm 0.1$. The slope of the experimental value $\eta = -2.55$ reported by Tallakstad et al. [6], has been added for comparison.

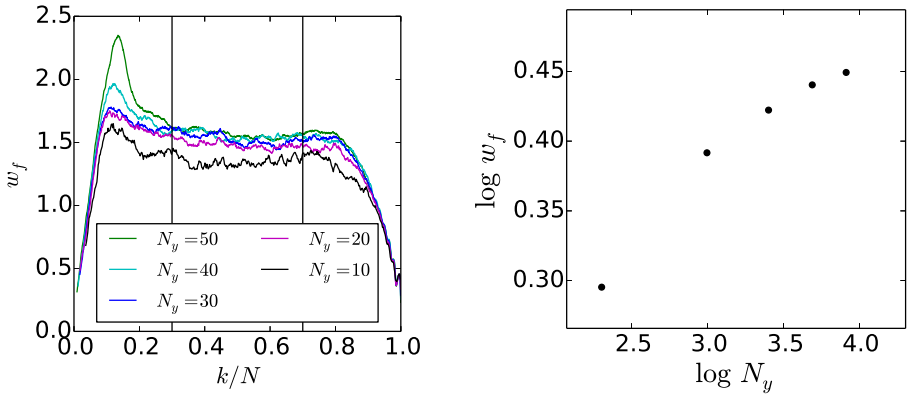

(a) **(b)**

Figure 4.13: The system size dependence of the width for $\beta = 10^{-3}$ is shown in **(a)**. The sampling region used is given by the vertical lines and results in the log-log plot shown in **(b)**. A linear fit to the points gave a slope ≈ 0.2.

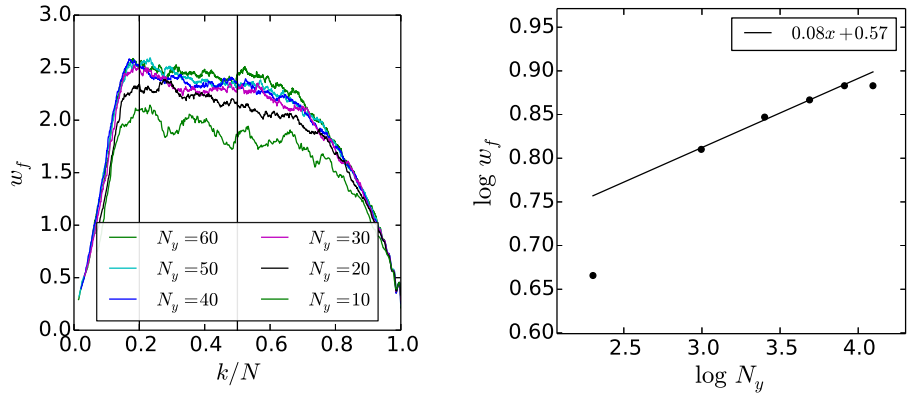

(a) **(b)**

Figure 4.14: The system size dependence of the width for $\beta = 10^{-4}$ is shown in **(a)**. The sampling region used is given by the vertical lines and results in the log-log plot shown in **(b)**. A linear fit to the points gave a slope ≈ 0.1.

4.3 Hinged Boundary Conditions

This section provides the results obtained by using the hinged boundary conditions given by Eqs. (3.4). The number of instances run for the different system parameters is shown in Table 4.2.

Table 4.2: The number of samples simulated for the Hinged Bridge model using $\beta = 10^{-5}$, and system sizes $N_x \times N_y = 50 \times N_y$. The presented quantities are averaged over the number of samples displayed in this table.

N_y	# of samples
10	100
20	100
30	100
40	100
50	100
60	20

The geometry of the Hinged Bridge model for softer systems is more or less identical to the fixed boundary system, given in Figure 4.3. The difference starts to show for stiffer systems, like illustrated for $\beta = 10^{-5}$ in Figure 4.15.

As a visual test, an ELS model with a gradient in the thresholds was constructed for comparison. The gradient weighted ELS should be equivalent to gradient percolation [21]. It was assumed that if gradient percolation can be physically interpreted as a stiff plate pulled downwards, then the Hinged Bridge model should provide the same result for low values of β. Figure 4.18 shows snapshots from a simulation comparing the Hinged Bridge model to the gradient system using the same threshold values. This was done for both $\beta = 10^{-5}$ and $\beta = 10^{-10}$.

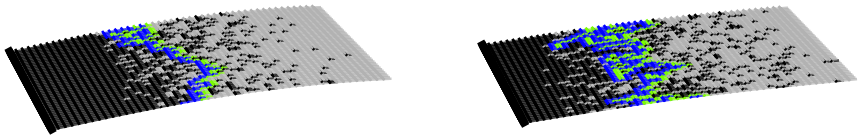

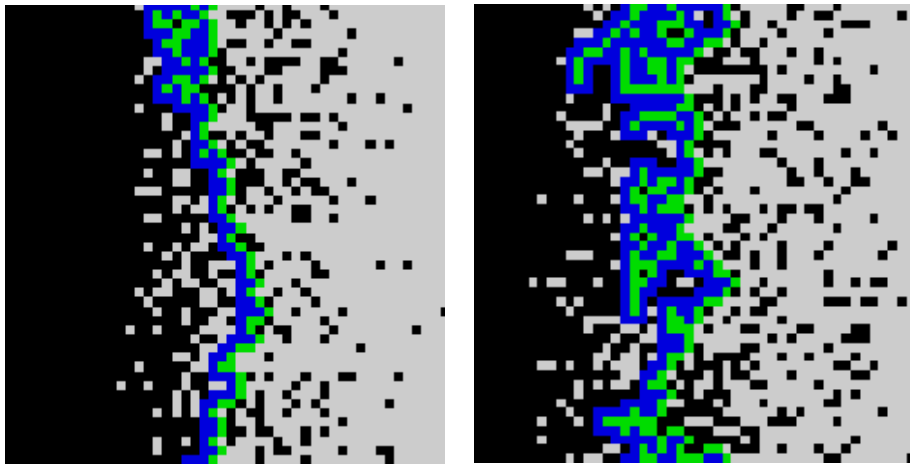

(a) Fixed Boundary **(b)** Hinged Boundary

Figure 4.15: Simulation snapshots of the front geometry with $\beta = 10^{-5}$ for both the fixed **(a)** and hinged **(b)** boundary. The 3D representation of the thin plate is shown above.

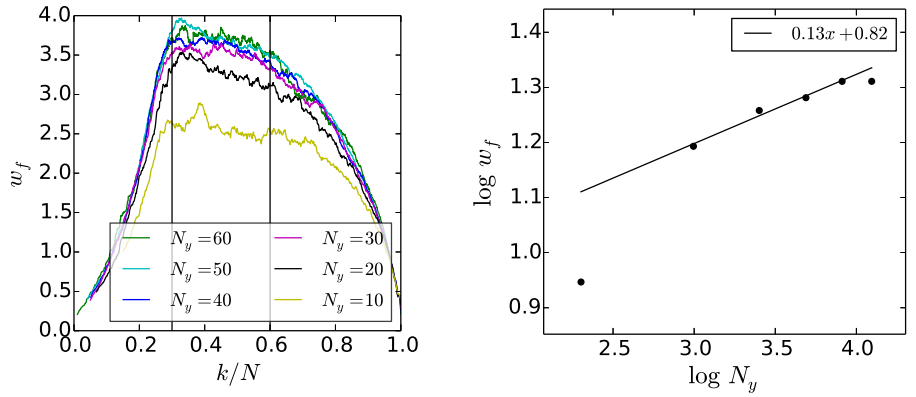

(a) **(b)**

Figure 4.16: The widths for different system sizes using the hinged boundary conditions with $\beta = 10^{-5}$. **(a)** shows the sampling region used to obtain the log-log-space of **(b)**. Many different sampling regions were tested, but the data is noisy and does not show a stable behavior. A linear regression of the points in the log-log plot indicated a slope ≈ 0.1.

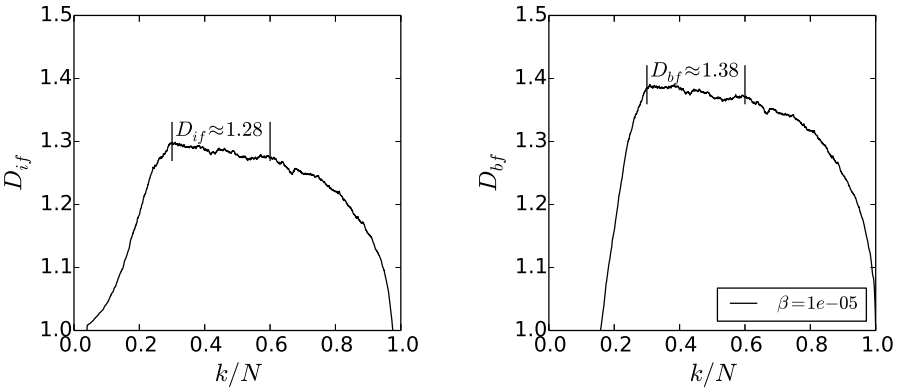

(a) **(b)**

Figure 4.17: The fractal dimension for the broken and intact front using hinge boundary conditions and $\beta = 10^{-5}$. No clearly stable region is visible, but a slightly flat region is used to estimate the fractal dimension.

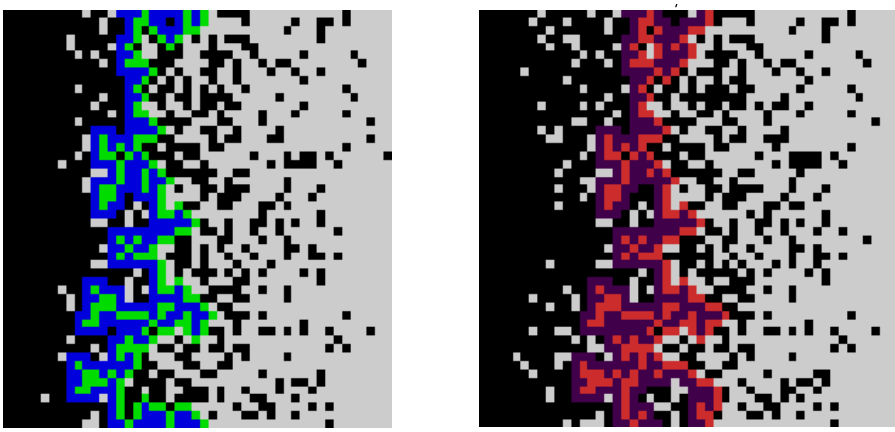

(a) $\beta = 10^{-5}$

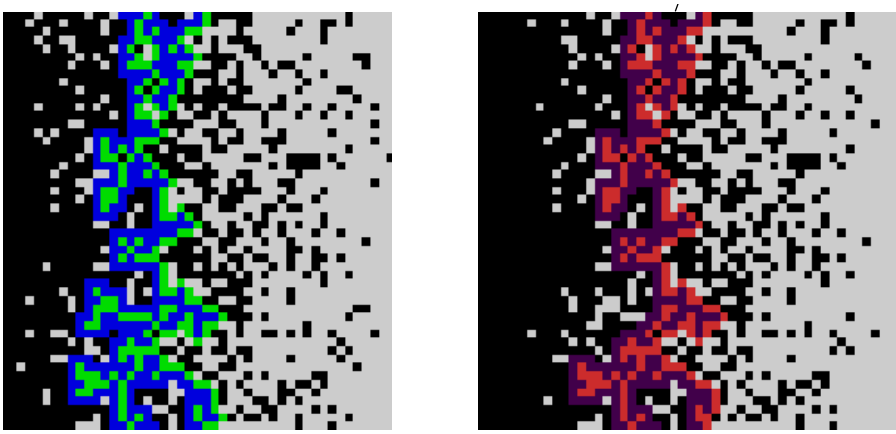

(b) $\beta = 10^{-10}$

Figure 4.18: Hinged Bridge model versus ELS with gradient in the threshold, presumably equivalent to gradient percolation. The different simulations use the same seed and obtain the same threshold values in order to compare the differences in the breaking order of the fibers. The snapshots are from two simulations with different values of β: **(a)** with $\beta = 10^{-5}$; and **(b)** with $\beta = 10^{-10}$. The snapshots were taken at $k/N \approx 0.5$. The colors representation of the Hinged Bridge model (left) is the same as in Figure 4.1, while the broken and intact front of the gradient percolation process (right) is shown in purple and red, respectively. Full movies of the process should be available with the thesis.

Chapter 5

Discussion

5.1 Front Definitions

The behavior different definitions for positions of the intact and broken front, x_{if}, x_{bf}, their average $\tilde{x}_f$ and the weighted position x_f behave as expected. The intact and broken front are located on either side of the actual interface, and this also holds true for their average positions. The x_{bf} is always located to the left of x_{if}, roughly one pixel away. This is clearly seen in Figure 4.2b. One can also see that the weighted front x_f is closer to the broken front compared to $\tilde{x}_f$. This is simply because the broken front is longer due to the constraint of nearest-neighbor connections, giving it more weights in Eq. (3.1) opposed to the intact front. The difference in length is given in Figure 4.7.
Exactly the same behavior is seen for $\tilde{w}_f$ and w_f regarding the widths of the front, shown in Figures 4.2c and 4.2d. However, here it is worth noting that w_{bf} is smaller than w_{if}. This is believed to be caused from the larger number of constituents in the broken front. This is also reflected in the length and fractal dimension, resulting in larger values for the broken front.

5.2 Change of Boundaries

The initial motivation of fixing the right end to be horizontal was the eventual window solver. It was thought that as long as the window solver was able to include the entire deforming region of the thin plate, as illustrated

in Figure 3.2, the interactions with the boundary would be minimal and should be able to produce reasonable results. This was ensured by evaluating the deformations for the 100×10 system in Figure 4.1, before choosing the values of β to be simulated. The estimated limit of $\beta = 10^{-3}$ seems to fit nicely with the obtained results, as stable reasonably stable regions are obtained. Anything higher than this however, for instance $\beta = 10^{-4}$, seem to interact increasingly with the boundary at $x = N_x - 1$. This is apparent from the strain curve, Figure 4.4, which shows that the applied load diverges as it needs to fight against the boundary, bending the plate.

Looking at Figure 4.3, one can see how the rigidity of the system decides how much the plate is allowed to bend. The sharper the bend, the more localised the fracturing region becomes. Within the fracturing region, the fibers appeared to break randomly. As β approaches 0, the system is expected to become so stiff that the bend would simply straighten out and the fracturing process should become unlocalised, leaving the fibers to break randomly over the entirety of the system, like gradient percolation. This should also be the effect when one magnifies the fracture front, looking at smaller scales, like illustrated in Figure 5.1. However, as illustrated in

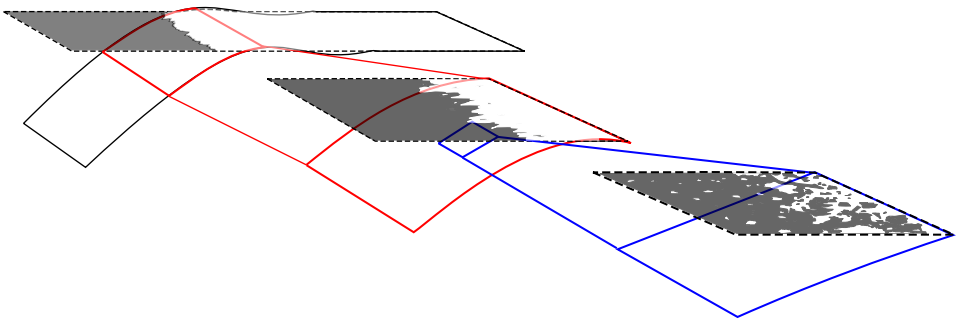

Figure 5.1: Decreasing β should be equivalent to evaluate the fracturing process on smaller scales. On extremely small scales, the thin plate clamp is expected to look flat, just like the surface of the Earth appears flat on small scales. Due to the applied load, the clamp should also be tilted. In this Figure, white represents intact fibers extended between the horizontal plane and the thin plate clamp.

Figure 3.5 and demonstrated by Figure 4.15, this sort of behavior does not seem to occur for a system with horizontally fixed boundaries. The plate seems to always be subject to bending, no matter how stiff the plate becomes. The only thing that seems to change, is the required load in order to

bend it. This is backed up by the diverging force in Figure 4.4. Presumably, if there is a bend, there is localisation. If the small scale roughness exponents only appears for unlocalised percolation, it was presumed that the fixed boundary Bridge Model would not be able to reproduce it, and motivated the change of boundary conditions. However, the results obtained using the fixed boundary conditions in the soft regime should still be valid for both boundary conditions due to the sort range of interaction given in this regime.

5.3 The Front Evolution and Initial Pinning for Soft Systems

For soft systems, the pinning regimes in Figure 4.5 illustrates that the front is pinned down by a few fibers still connected to the left edge of the system. The rest of the front continues inwards until it gets pinned down again, roughly half-way into the system. This is shown in Figure 4.5 at the pinning regime of $C = 10$. Here the front stays while the arm that connects the intact cluster to the left boundary, is eaten up from either side. At some point it finally releases and results in the large valued depinning cluster shown to the middle left of all the depinning threshold maps. After this, the front stabilizes and remains stabilized the rest of the simulation.

This behavior seem to happen for every instance of a soft system and manifest itself into the results by showing an increase in the front width, Figure 4.6b, the length, Figure 4.7, and followingly the fractal dimension, Figure 4.8 and prevents a approximate one parameter description $w_f(x_f)$ given in Figure 4.10. These quantities peak when the front is pinned down half-way into the system by the remaining arm. As soon as the arm dissolves, the fronts straighten out and cause the sharp drop in the width and length of the front. This also causes the behavior of the position x_f shown in the lower inset of 4.6a. As the front is slowed down, the function drops below the linear behavior. As the front is released from the left edge, the average position speeds up, causing a steep rise back to the diagonal where it stabilizes at constant speed. The linear behavior of x_f with the clock of breaking fibers k is an analogous result to the ballistic deposition model [35, p.20] and shows consistency with Eq. (2.46).

The observed initial pinning of soft systems pose a problem as it reduces the stable region which is used to estimate the roughness exponent. At this point, 40% of the simulation is lost to the growth and stabilization of the front. Looking at peak in Figure 4.9a, the peak increases with the width of the system. This might indicate that the time of stabilization of the front has something to do with the correlation length of the system, revealing itself as a finite size effect.

A more practical explanation, is that pinning is caused by the way the system is loaded. The system is loaded only by introducing a gravitational force only on the edge beam. This edge beam is just as soft as the rest of the system. This seems to allow a few strong edge fibers remain as nothing constrains the weighted beam to be at the same height. The weight of the small section above the remaining edge fibers is therefore not enough to break them before breaking weaker fibers further into the system. If this reasoning is true, this would mean that increasing the stiffness of the loaded beam would prevent this initial pinning and lead to an earlier stabilization of the front. This is further backed up by the reduced effect of the initial pinning for stiffer systems and is almost gone for $\beta = 10^{-4}$. Another approach that was attempted without changing the model, was to remove the first columns of fibers, creating a gap between the edge of the system and the intact front. From a few test simulations, this seemed to move the stabilization time from $k/N \approx 0.4$ to $k/N \approx 0.2$. Some snapshots of this is shown in Appendix D.

5.4 The Velocity Distribution

By sampling the stable region $k/N \in [0.5, 0.95]$, visible in the width for $\beta = 1$ in Figure 4.6b, the velocity distribution given in Figure 4.12. It should be noted that not including the effect of the variations of the global velocities illustrated in Figure , give a slightly different result. The velocity distributions of both the intact and the broken, $p_{if}(v/\langle v \rangle)$ and $p_{bf}(v/\langle v \rangle)$, peak in the pinning regime. However, only the peak position of $p_{bf}(v/\langle v \rangle)$ is consistent with the experimental results given by Tallakstad et al.[6]. The high velocity tail of the broken front also seems to follow a power law, as reported [6]. However, the numerically obtained exponent $\eta_{bf} \approx 0.65 \pm$

0.07, does no match with the experimentally measured power law exponent of $\eta = -2.55 \pm 0.15$. The reason for this, is at the time of writing, not known by the author, but could be due to the relatively small size of the system.

5.5 The Fractal Dimension

The fractal dimension in Figure 4.8, shows that the $D_{if} \approx 1$ for the softest system of $\beta = 1$. However, D_{bf} is not not close to 1. This is because the intact front is not constrained by nearest-neighbor connections, and may therefore deform without necessarily causing an increase in its length. For instance, a 45° angled pixelated line would have the same number of pixels as a line drawn straight up. Going on, as the stiffness of the system increases, the fracture dimension increases. This might indicate that coalescence of small holes begin to contribute to the propagation of the front leading to rougher and rougher surfaces as larger and larger clusters start to merge with the front, eventually leading to a fractal dimension of $D_f = 4/3$, described by gradient percolation [42], indicating an extremely stiff system. Looking at Figure 4.3, one can see how the contribution from coalescence gradually increases with the stiffness of the system. As the stiffness reaches $\beta = 10^{-5}$, the front is no longer stable. However, the fractal dimension of the most stable region, shown in Figure 4.17, is just slightly above and below the fractal dimension of gradient percolation, indicating that the front is primarily driven forward by percolation.

It is worth noting that, although the Bridge model approaches LLS qualitatively for $\beta \sim 1$ in one dimension [12], it does not do so in two dimensions. The fractal dimension for a broken front governed by localized LLS [17] or *invasion percolation* [43] should have a value of $D_{bf} = 4/3$, the same as for gradient percolation. However, the softest system in the Bridge Model, given by $\beta = 1$, only provides $D_{bf} \approx 1.1$. This may be due to the fact that LLS does not care about the shape of a hole but only about its size, see Eq. (2.7). This allows for LLS to invade regions of weak fibers and carve out a highly fractal geometry. The Bridge Model on the other hand, seem exert such a strong force on the fibers closest to the hole, that these fibers are more likely to break, resulting the relatively smooth fracture surface with $D_f \approx 1$.

5.6 The Roughness Exponent

The estimated roughness exponent of $\zeta = 0.27 \pm 0.06$ from Figure 4.9 is somewhat lower than the experimentally obtained value of $\zeta_{large} = 0.35 \pm 0.05$ from Santucci et al. [7], but is still considered to be consistent with a large scale roughness exponent. Compared to the numerical value of $\zeta = 0.39 \pm 0.04$, obtained by Gjerden using a thick block [3], this value ends up on the other end of the experimental value. It is tempting to assume that this difference results from the application of a thin plate versus a thick block clamp model. However, with the small systems considered in the model together with relatively few samples at this point not possible to say if there is a difference.

The Family-Vicsek scaling given in Figure 4.10, gave a best fitting for a dynamic exponent of $Z = 0.45 \pm 0.09$. Measuring the angle of the slope gave the growth exponent of $b = 0.5 \pm 0.1$. This result is not completely consistent with Eq. (2.50), giving a error of roughly 20%. A one parameter description of the curve was however not obtained due to the initial pinning of the softer systems.

Estimations of the roughness exponent for the stiff systems, such as $\beta = 10^{-3}$ and $\beta = 10^{-4}$, using Eq. (2.44), was also attempted. This is shown in Figure 4.13 and 4.14, respectively, but did not give a positive result. It was believed to either be because the systems where in the crossover region between the two regimes or that the fixed boundary forced a localising behavior onto the system. This was a part of the motivation for changing the boundary conditions. However, the change of boundaries did not seem to make a huge difference, which can be seen from the attempted power law estimation in Figure 4.16. The front does not form a properly stable region and the fluctuations are not averaged out. However, in Figure 4.18, a comparison of with a ELS system with a gradient in the threshold, which should be equivalent to the gradient percolation problem investigated by Hansen et al. [21], one can see that the morphology is almost identical. This similarity is better for $\beta = 10^{-10}$ than $\beta = 10^{-5}$, as expected. Although the morphology of the simulated percolation process was not analysed, it is expected to be similar to the analysed result for $\beta = 10^{-5}$, meaning Figures 4.16 and 4.17. It is therefore presumed that the failure of estimating the roughness exponent in the stiff regime, is due to the small system

sizes considered. However, because the behavior of the system seems to be qualitatively consistent with gradient percolation, as shown from both the fractal dimension in Figure 4.17 and visually based on the simulation in Figure 4.18, it is assumed to also be consistent with a roughness exponent of $\zeta_{small} = 2 - D_f = 2/3$ [21].

Chapter 6

Conclusion

Although the boundary conditions were changed in the middle of the process in order to obtain a reasonable result for the small scale behavior, the large scale behavior of the different boundary conditions should be the same. This is because the interaction length for the soft systems is so small that the fixed or hinged boundary is not affecting the result. It is therefore advised to use the Hinged boundary conditions for future research of the model.

Summarized, this paper derived a new, history independent, thin plate Fiber Bundle Model, used for modelling mode I, in-plane fracture front propagation. The model is based on the Bridge Model of Nygård [12], and has a tunable range of interaction by altering the stiffness of the plate. Due to the small system sizes and relatively small ensembles considered in this paper, any comparison with the results of the Soft Clamp Model obtained by Gjerden for a infinitely thick plate [3], is not possible due to inadequate data.

In the soft regime, a roughness exponent of $\zeta = 0.27 \pm 0.06$ was found, and is assumed to be consistent with the large scale exponent measured by Santucci et al. [7]. This behavior is believed to arise from the localisation of the force as the plate softens. In the stiff regime, no numerical value for the roughness exponent was achieved. However, with a fractal dimension consistent with $D_f = 4/3$ and by visual comparison with gradient percolation, the system is believed to be consistent with the small scale roughness exponent $\zeta_{small} = 2/3$, described by gradient percolation [21].

The high velocity tail of the velocity distribution for the broken front, seemed to be consistent with a power law, with an exponent of

$$\eta_{bf} = -0.75 \pm 0.07.$$

This is, however, not consistent with the experimental value reported by Tallakstad et al. [6].

Future work

The most obvious next step for future work, would be to find a better solution for the matrix problem. For instance, one could try to implement a better iterative solver by using CG with a proper preconditioner to speed up convergence.

Another important step, would be to implement a window solver, solving for only a subset of the system. Reducing the size of the matrix is essential for speeding up the process. For soft enough systems, it is believed to be adequate to only solve for the region containing the deformations of the plate, as discussed in this thesis. However, for stiff systems, the interactions are presumed to always interact with the boundary, as the range should approach infinity. In this case, one would need to be clever with the choice of the boundaries. Perhaps one can implement a boundary with adjustable slope and height. In order to be able to cut off the completely broken region of fibers, one would need to check whether or not the load can be moved and still obtain the same statistical result. A statistical analysis of the movable load could therefore be compared to the statistical data of an entire system, ant comparing that the obtained quantities are statistically equivalent. If this is successful , one could try to remove the parts of the clamp below the completely broken region, and check if the results are compatible with everything else.

If a better solver is achiever, then larger systems and larger ensembles could be considered. Hopefully, if the statistical data is good enough, a proper comparison to the SCFBM could have been made.

Bibliography

[1] P Thompson. How much did the liberty shipbuilders learn? new evidence for an old case study. *Journal of Political Economy*, 109(1):103, 2001.

[2] A Almar-Næss, PJ Haagensen, B Lian, T Moan, and T Simonsen. Investigation of the alexander l. kielland failuremetallurgical and fracture analysis. *Journal of energy resources technology*, 106(1):24, 1984.

[3] KS Gjerden. *Role of the quenched disorder in fracture front propagation*. NTNU. Ph.D. Thesis. 2013.

[4] BB Mandelbrot, DE Passoja, and AJ Paullay. Fractal character of fracture surfaces of metals. 1984.

[5] J Schmittbuhl and KJ Måløy. Direct observation of a self-affine crack propagation. *Physical review letters*, 78(20):3888, 1997.

[6] KT Tallakstad, R Toussaint, S Santucci, J Schmittbuhl, and KJ Måløy. Local dynamics of a randomly pinned crack front during creep and forced propagation: An experimental study. *Physical Review E*, 83(4):046108, 2011.

[7] S Santucci, M Grob, R Toussaint, J Schmittbuhl, A Hansen, and KJ Maløy. Fracture roughness scaling: A case study on planar cracks. *Europhysics Letters*, 92(4):44001, 2010.

[8] A Hansen, PC Hemmer, and S Pradhan. *The Fiber Bundle Model: Modeling Failure in Materials*. John Wiley & Sons, 2015.

[9] F Kun, F Raischel, RC Hidalgo, and HJ Herrmann. Extensions of fibre bundle models. In *Modelling Critical and Catastrophic Phenomena in Geoscience*, page 57. Springer, 2006.

[10] GG Batrouni, A Hansen, and J Schmittbuhl. Heterogeneous interfacial failure between two elastic blocks. *Physical Review E*, 65(3):036126, 2002.

[11] J Schmittbuhl, A Hansen, and GG Batrouni. Roughness of interfacial crack fronts: stress-weighted percolation in the damage zone. *Physical review letters*, 90(4):045505, 2003.

[12] HT Nygård. *The Fiber Bundle Bridge Model*. NTNU. Specialization Project (unpublished). 2016.

[13] FT Peirce. Tensile tests for cotton yarns–the weakest link theorems on the strength of long and of composite specimens. *Journal of the Textile Institute*, 17:T355, 1926.

[14] HE Daniels. The statistical theory of the strength of bundles of threads. i. 183(995):405–435, 1945.

[15] P Bhattacharyya and BK Chakrabarti. *Modelling critical and catastrophic phenomena in geoscience: a statistical physics approach*, volume 705. Springer, 2006.

[16] JT Kjellstadli. *Investigating the Local Load Sharing Fibre Bundle Model in Higher Dimensions*. NTNU. M.Sc. Thesis. 2015.

[17] M Dahle. *Critical Behaviour of the Local Load Sharing Fiber Bundle Model*. NTNU. M.Sc. Thesis. 2016.

[18] S Sinha, JT Kjellstadli, and A Hansen. Local load-sharing fiber bundle model in higher dimensions. *Physical Review E*, 92(2):020401, 2015.

[19] A Yavari, S Sarkani, and ET Moyer. On applications of generalized functions to beam bending problems. *International Journal of Solids and Structures*, 37(40):5675, 2000.

[20] J Hoshen and R Kopelman. Percolation and cluster distribution. i. cluster multiple labeling technique and critical concentration algorithm. *Physical Review B*, 14(8):3438, 1976.

[21] A Hansen, GG Batrouni, T Ramstad, and J Schmittbuhl. Self-affinity in the gradient percolation problem. *Physical Review E*, 75(3):030102, 2007.

[22] BB Mandelbrot. How long is the coast of britain. *Science*, 156(3775):636, 1967.

[23] M Joyce, FS Labini, A Gabrielli, M Montuori, and L Pietronero. Basic properties of galaxy clustering in the light of recent results from the sloan digital sky survey. *Astronomy & Astrophysics*, 443(1):11, 2005.

[24] J Feder. *Fractals*. Springer Science & Business Media, 2013.

[25] EH Hauge. *Go Critical*. (unpublished), NTNU, 2001.

[26] JS Geronimo and DP Hardin. An exact formula for the measure dimensions associated with a class of piecewise linear maps. page 89, 1989.

[27] TH Wilson. Some distinctions between self-similar and self-affine estimates of fractal dimension with case history. *Mathematical geology*, 32(3):319, 2000.

[28] F Family and T Vicsek. Scaling of the active zone in the eden process on percolation networks and the ballistic deposition model. *Journal of Physics A: Mathematical and General*, 18(2):L75, 1985.

[29] BB Mandelbrot. *The Fractal Geometry of Nature*. WH Freeman, 1982.

[30] HE Stanley. *Introduction to phase transitions and critical phenomena*, volume 1. 1987.

[31] JG Brankov, DM Danchev, and NS Tonchev. *Theory of critical phenomena in finite-size systems: scaling and quantum effects*, volume 9. World Scientific, 2000.

[32] E Bouchaud, JP Bouchaud, DS Fisher, S Ramanathan, and JR Rice. Can crack front waves explain the roughness of cracks? *Journal of the Mechanics and Physics of Solids*, 50(8):1703, 2002.

[33] J Schmittbuhl, S Roux, JP Vilotte, and KJ Måløy. Interfacial crack pinning: effect of nonlocal interactions. *Physical Review Letters*, 74(10):1787, 1995.

[34] KS Gjerden, A Stormo, and A Hansen. Universality classes in constrained crack growth. *Physical review letters*, 111(13):135502, 2013.

[35] A-L Barabási and HE Stanley. *Fractal concepts in surface growth*. Cambridge university press, 1995.

[36] G et al. Marsaglia. Xorshift rngs. *Journal of Statistical Software*, 8(14):1, 2003.

[37] S Vigna. An experimental exploration of marsaglia's xorshift generators, scrambled. *arXiv preprint arXiv:1402.6246*, 2014.

[38] C Sanderson. Armadillo: An open source c++ linear algebra library for fast prototyping and computationally intensive experiments. 2010.

[39] M Rosso, JF Gouyet, and B Sapoval. Determination of percolation probability from the use of a concentration gradient. *Physical Review B*, 32(9):6053, 1985.

[40] B Sapoval, M Rosso, and JF Gouyet. The fractal nature of a diffusion front and the relation to percolation. *Journal de Physique Lettres*, 46(4):149, 1985.

[41] KJ Måløy, S Santucci, J Schmittbuhl, and R Toussaint. Local waiting time fluctuations along a randomly pinned crack front. *Physical review letters*, 96(4):045501, 2006.

[42] T Grossman and A Aharony. Accessible external perimeters of percolation clusters. *Journal of Physics A: Mathematical and General*, 20(17):L1193, 1987.

[43] D Stauffer and A Aharony. Introduction to percolation theory. 2nd edtaylor and francis. *181pp*, 1992.

Appendix

Write your appendix here...

A The breaking criteria

Because the breaking criteria is an important aspect of the model, it should be explained more carefully in order to avoid confusion. To be absolutely clear, the notation for fiber j is such that, t_j gives the threshold, x_j gives its extension due to the local force σ_j, while $\sigma = F/N$ is the total force on the bundle rescaled by N. N is the initial number of fibers in the bundle. Due

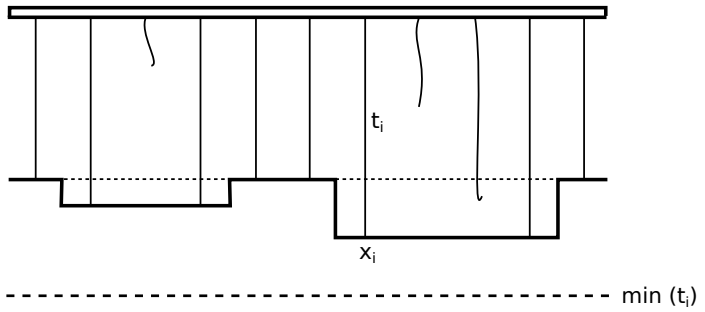

Figure A.1: The fibers extensions x_i due to the load σ_i resulting from the holes in LLS.

to the load distribution, the extension of the fiber is decided through

$$\sigma_j = \kappa_j x_j, \tag{6.1}$$

where σ_j is given by Eq. (2.7) for LLS. Similarly, x_j would be found by solving the matrix problem in the bridge model. If σ is so low that every

intact fiber i is far from breaking, see Figure A.1, then

$$t_i \geq x_i = \frac{\sigma_i}{\kappa}, \tag{6.2}$$

which can be rewritten to

$$1 \geq \frac{\sigma_i}{t_i \kappa}. \tag{6.3}$$

Now, the fiber whose factor reaches $\sigma_i / t_i \kappa = 1$ first when the load is increased, is the first fiber to satisfy Eq. (6.2). This means that the fiber breaks. The reason this works is because σ_i is linearly dependent on the applied load σ and results in that

$$\max_i \left\{ \frac{\sigma_i}{t_i \kappa} \right\} \tag{6.4}$$

gives the first fiber i of the remaining configuration of fibers that will break when σ is increased.

A.1 Bridge model breaking criteria under the influence of gravity

Using a non-zero gravity term, $\alpha \neq 0$, and loading the system by increasing α_L gives a local displacement of a node is given by $d_{kl}(\alpha_L) = S_{kl}\alpha_L + C_{kl}$. This is illustrated in Figure A.2, which also shows the displacement relation when $\alpha = 0$. In order to decide both S_{kl} and C_{kl}, the system needs to be solved for two different values of α_L, say for $\alpha_L^{(0)}$ and $\alpha_L^{(1)}$, leading to a total of $2N$ iterations of solving the matrix in order to simulate the rupture of the entire system. With the two solutions, the slope is given

$$s_{kl} = \frac{d_{kl}^{(1)} - d_{kl}^{(0)}}{\alpha_L^{(1)} - \alpha_L^{(0)}},$$

and for the load as a function of the displacement, the result is

$$\alpha_L' = \alpha_L^{(0)} + \Delta\alpha_L = \alpha_L^{(0)} + \frac{1}{s_{kl}}\Delta d_{kl} = \alpha_L^{(0)} + \frac{\alpha_L^{(1)} - \alpha_L^{(0)}}{d_{kl}^{(1)} - d_{kl}^{(0)}}\left(d_{kl} - d_{kl}^{(0)}\right).$$

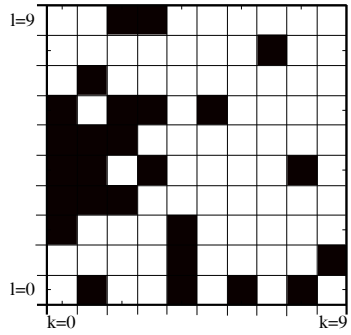

(a)

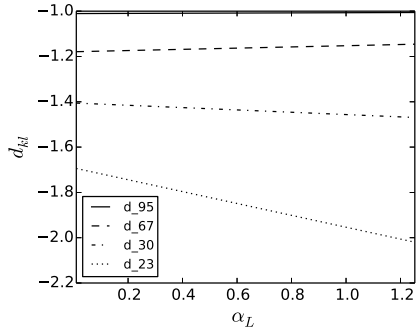

(b)

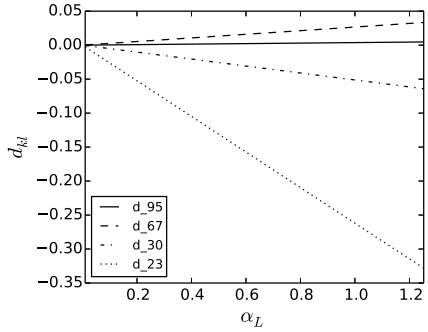

(c)

Figure A.2: For the given configuration of broken (black) and intact (white) fibers of a 10×10 system shown in **(a)**, the load α_L was increased. The resulting local displacement d_{kl} of 4 randomly chosen nodes is shown for **(b)** uniform load, $\alpha = 0.1$, and **(c)** no uniform load, $\alpha = 0$. In this calculation, $\beta = 0.2$.

The first fiber to break in this case, is when

$$\min_{k,l} \left| \frac{t_{kl} - d_{kl}^{(0)}}{d_{kl}^{(1)} - d_{kl}^{(0)}} \right| \tag{6.5}$$

In order to guarantee that the fibers are forced to break only in the downward direction one can demand that the change in displacement of the two solutions $\Delta d_{kl} < 0$, which, by replacing the $\min\{\}$-term in Eq.6.5 with

$\max\{\}$, gives

$$\alpha'_L = \max_{\left\{k,l:\, d_{kl}^{(1)} - d_{kl}^{(0)} < 0\right\}} \left| \frac{d_{kl}^{(1)} - d_{kl}^{(0)}}{t_{kl} - d_{kl}^{(0)}} \right| \alpha_L, \tag{6.6}$$

B Finding the front; step-by-step

B.1 Cluster labeling

The clusters were labeled using the Hoshen-Kopelman algorithm [20]. where the labels of the fiber configuration are stored in a so-called cluster label matrix. When a fiber breaks, it is labeled by its index in the label matrix. If the broken fiber is neighboring any other lone broken fibers, then their index is changed to the index of the recently broken fiber. In this way, the fibers are connected together into a small cluster and all of them are labeled by the index of the newly broken fiber. The newly broken fiber is now called the root of the cluster, because every fiber in the cluster can point to it by dereferencing their own label into the cluster label matrix.
Now, if a fiber that is neighboring the cluster breaks, one does not need to change all the labels of the cluster. Instead the label of the neighboring cluster fiber is dereferenced in order to find the root and only the root is changed. The original root of the cluster is now no longer the current root, and the cluster now contains different labelled fibers. However, the root connects all the fibers in the cluster, because they can all point to it. If again, another fiber bordering to the cluster breaks, it takes the bordering label to get to the previous root and uses the previous root in order to reach the current root. The current root is then changed making the broken fiber the new root. Summarized one can say that, each time a fiber breaks it is made the root of all the neighboring clusters and in this way connects them. A summary of the algorithm is shown in the following pseudo code.

```
//When breaking fiber i:
clusterLabelMatrix[i] = i
for ineighbor = [iup,iright,idown,ileft]:
    if(neighborIsBroken(ineighbor)):
        nextLabel = clusterLabelMatrix[ineighbor]
        while(nextLabel != clusterLabelMatrix[nextLabel]):
            nextLabel == clusterLabelMatrix[nextLabel]
        root = nextLabel
        clusterLabelMatrix[root] = i
```

If a common cluster label is desired, the fiber labels are looped over and set to their root label. Figure B.1 shows an example of the algorithm. Note that the labels depend on the breaking order of the fibers.

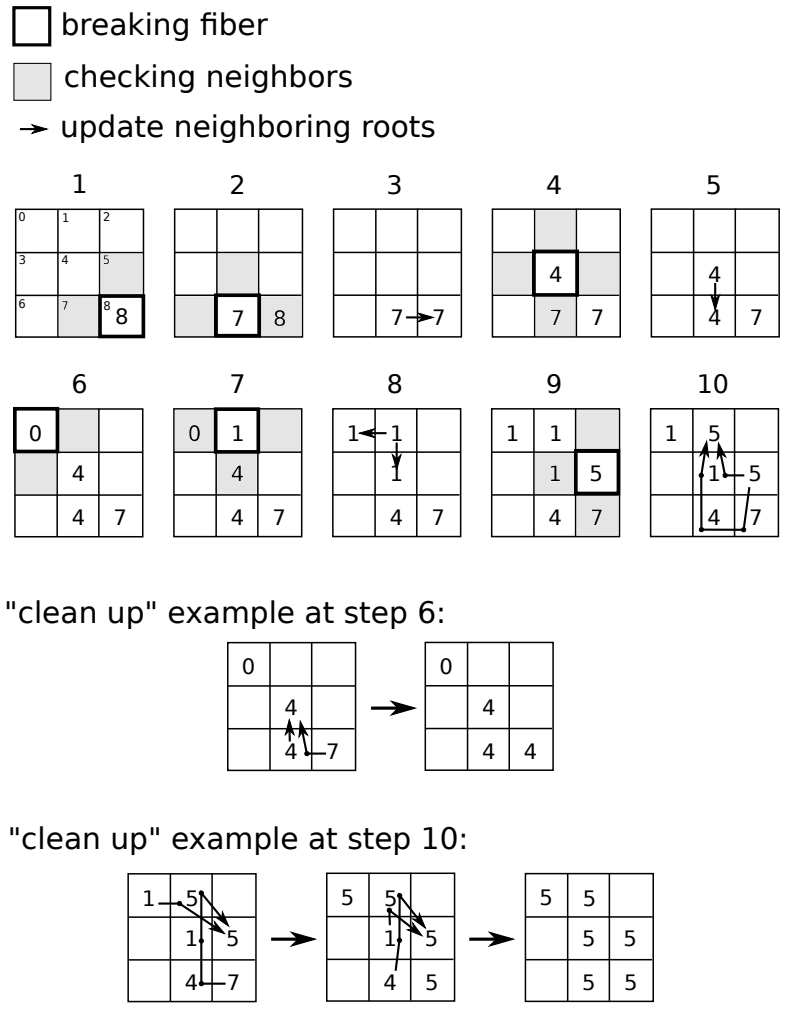

Figure B.1: A visualisation of the algorithm for a 3×3 cluster label matrix when the breaking order of the fibers is $\{8, 7, 4, 0, 1, 5\}$. The 2D lattice is labeled by a one-dimensional index. At step 10, the neighboring labels do not match their index, i.e. they are not the root of the neighboring cluster. Following the labels, the root of the neighboring cluster is found and relabeled.

B.2 The void cluster

After all the clusters have been labeled, all the clusters constituting the void cluster are found by running up along the left edge at $x = 0$.

B.3 The reduced front

The reduced front is simply found by running right-to-left along every row until the void cluster is encountered.

B.4 The broken and intact front

The algorithm for finding both the broken and intact front, is neatly explained by Dahle [17]. However, for completeness, it will be recapitulated here: The following steps assumes that the void cluster has already been labeled:

1. The first member of the broken front is found by choosing an arbitrary row $r \in [0, N_y - 1]$, where one runs left-to-right until the first member of the void cluster is found. This is the starting point. Save this as the starting position p_s.

2. Enumerate the directions up[0], right[1], down[2] and left[3] and initialize the walking direction and arriving direction to up, $d_{next} = d_{prev} = 0$.

3. Define $d_{next} = (d_{prev} + 1 - q) \ \% \ 4$, where the modulo indicates periodic addition, i.e. ensures that $d_{next} \in [0, 1, 2, 3]$.

4. Always start trying to walk to the right, given by $q = 0$. If this does not work because there is an intact fiber there, then check the next direction in a counterclockwise manner by checking $q = q + 1$ until a walkable direction is found. If this is the first step, then store the initial step direction $d_s = d_{next}$

5. Move in the walkable direction d_{next} and update $d_{prev} = d_{next}$, and label the current position x as part of the front.

6. Repeat the two previous steps until both $x == x_s$ and $d_{next} == d_s$ are satisfied. This means that one is back to the start and the entire broken cluster is labeled.

In order to label the intact front, one should note that every time a direction is not walkable it is because there is an intact fiber there. If it is not labeled, it is added to the intact front. This way, both the broken and intact fronts are found by one single walk along the interface. Finally, Figure B.2 shows how the resulting cluster label matrix, the reduced front and the full fonts of an example configuration of intact and broken fibers.

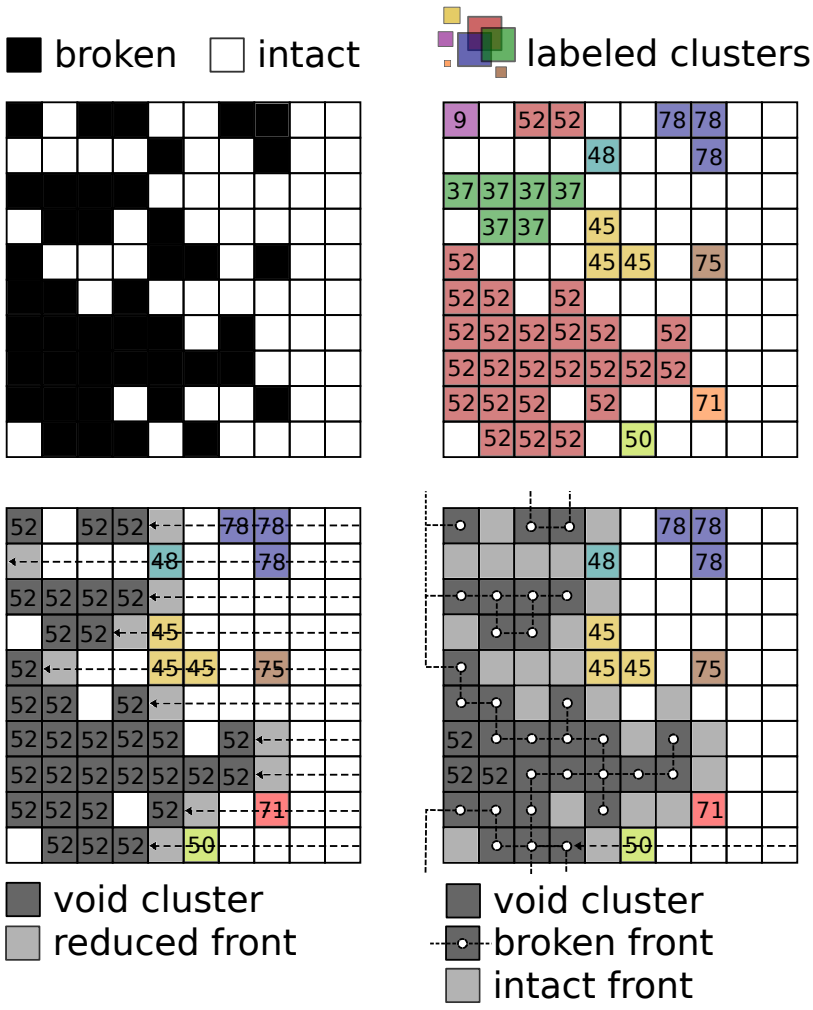

Figure B.2: the labeling of different clusters and fronts of a 10×10 fiber configuration shown to the upper left. Based on the different cluster labels, shown to the top right, the reduced front(lower left) and the full broken and intact front (lower right) could be found. When finding the different fronts, all the clusters constituting the "void-cluster" were given the same label as the first found edge cluster, here given by cluster 52. The reduced front were simply found by search for the void cluster right-to-left. Starting from an arbitrary chosen broken fiber to the left of the reduced front, the full intact and broken front can be found.

C Testing the movable load

In order to test if the movable load gave the same breaking order of the fibers as the stationairy load, some simulations using the same seed where compared up to one another. For one simulation, the load was held fixed at $x = 0$. This is referred to as the stationairy load. For the other simulations, the load was set to move everytime all fibers a distance d_{load} had broken. The resulting applied load is given in Figure C.1, where the fluctuations in the force seem to be the same but remains fairly constant when it moves after the front. In Figure C.1b, the relation between the moving and the stationairy load seems to be linear, and could allow for the force to be rescaled or renormalized if the movable load is used in a potential window solver. The scattering around the lines are believed to be due to the change in the breaking order of the fibers. This is illustrated in Figure C.2, which shows the configuration deviation histogram. At each time step, the moving load configuration of fibers is compared to the stationary configuration of fibers. If the fibers are in different states, the corresponding position of the histogram is incremented by 1.

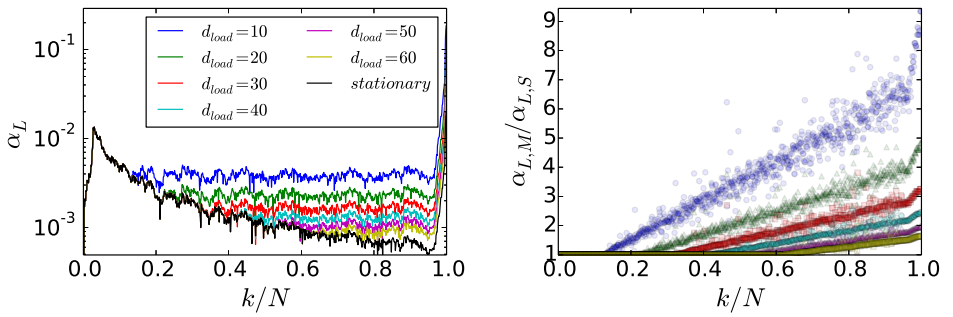

(a) **(b)**

Figure C.1: Simulations for 100x10 and $\beta = 10^{-2}$ using the same seed. **(a)** The load curves, $\alpha_L(k/N)$. **(b)** The relative required load to break a fiber for a moving load, $\alpha_{L,M}$, with distance d_{load} to the first intact fiber, compared to that of a stationary load, $\alpha_{L,S}$, located at $x = 0$.

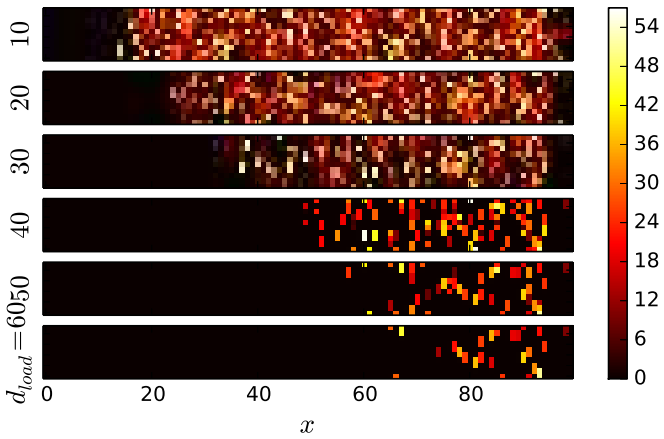

Figure C.2: The configuration deviation histogram for the situation shown in Figure C.1.

D Speeding up the front stabilization

In every simulation the front seemed to be pinned down by a strong fiber clinging to the left edge of the system. The softer the system is, the larger this effect becomes. Statistically, this causes a huge problem as the stable region of the front is drastically reduced. Due to the fact that it happens every single simulation, it seems as if the deformation of the system creates a point of very little stress and is allowed to happen because the loaded beam is just as soft as the rest of the system. If one removes all the intact fibers in the region $x \in [0, 4]$, the stabilization of the front seemed to occur at $k/N = 0.2$ instead of $k/N = 0.4$. This is shown in Figure D.1, It shows a test simulation where one start by breaking the first four columns of fibers. It is compared to a unchanged system that starts with breaking fibers at random.

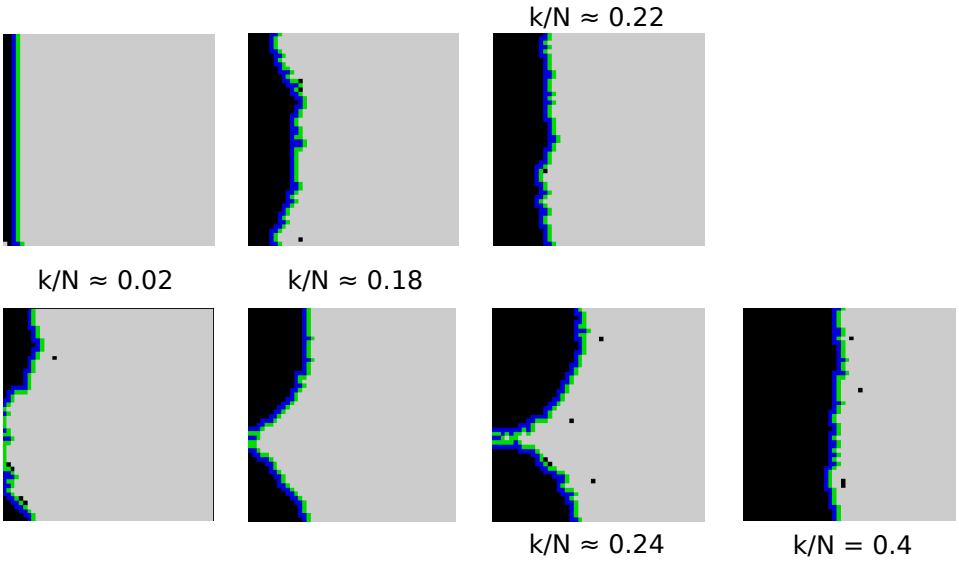

Figure D.1: Trying to obtain faster front stabilization for a 50×50 system with $\beta = 1$. The upper row of snapshots is from the test simulation where the four first columns of fibers are removed before the fracturing process commences. In this case the front stabilizes around $k/N \approx 0.2$. A normal simulation is shown for comparison. The pinning at the left edge of the system, causes the late stabilization at $k/N \approx 0.4$.